

## Development of permeable networks by viscous-brittle deformation in a shallow rhyolite intrusion. Part 2: Microstructural analysis

Taylor Witcher<sup>a,b</sup>, Steffi Burchardt<sup>a,b,\*</sup>, Tobias Mattsson<sup>a</sup>, Michael J. Heap<sup>c,d</sup>, Anne Pluymakers<sup>e</sup>, Kai Li<sup>e</sup>, Peter Lazor<sup>a</sup>

<sup>a</sup> Department of Earth Sciences, Uppsala University, Uppsala, Sweden

<sup>b</sup> Centre for Natural Hazards and Disaster Science, Sweden

<sup>c</sup> Institut Terre et Environnement de Strasbourg, Université de Strasbourg, CNRS, Strasbourg, France

<sup>d</sup> Institut Universitaire de France (IUF), Paris, France

<sup>e</sup> Department of Geoscience and Engineering, Technical University Delft, Delft, Netherlands

### ARTICLE INFO

#### Keywords:

Magma mush  
Outgassing  
Magma fracture  
Cavitation  
Sandfell laccolith  
Permeable network

### ABSTRACT

Volcanic and magmatic outgassing mechanisms can determine eruptive behavior of shallow silicic magma bodies. Most outgassing mechanisms proposed take place along conduit margins, where the highest strain rates drive ascending magma to brittle failure. However, these mechanisms do not account for outgassing large volumes of magma away from the conduit walls. Here, we present a continuum of porosity preserved in the microcrystalline rhyolitic Sandfell laccolith, Eastern Iceland. Three stages in the continuum are described: porous flow bands, pore channels, and fracture bands. These deformation features are present throughout the entire exposed volume of the Sandfell laccolith in meter-long band geometries, ranging from mm- to dm-scale thickness, and interlayered with coherent, undeformed rhyolite. Using microstructural analytical methods and drawing on the result of previous experimental studies, we show that emplacement-related deformation induced strain partitioning around a crystal content of 45 % that resulted in the segregation of melt-rich and melt-poorer flow bands. Subsequent deformation induced by continued magma emplacement caused strain partitioning in the melt-rich flow bands. Depending on strain rate, different types of deformation features developed, through dilation or porosity redistribution (porous flow bands), cavitation (pore channels), or tensile fracture (fracture bands). Porous flow bands have permeability values ~4 orders of magnitude higher than undeformed rhyolite. Pore channels and fracture bands have much larger length scales, and so permeability increases dramatically in those systems. Hence, the abundance and interconnectivity of deformation features preserved in the Sandfell laccolith provided an efficient outgassing mechanism for the bulk of the intrusion. Outgassing due to viscous-brittle magma deformation during magma emplacement should therefore be considered for crystal-rich magmas, e.g., during effusive lava dome extrusion.

### 1. Introduction

Degassing and outgassing of silicic magma in the shallow Earth's crust are key processes that affect the explosivity of volcanic eruptions because the efficiency with which volatiles move through and leave magma largely controls the pressure within the volcanic plumbing system (Colombier et al., 2022; Jaupart and Allègre, 1991; Rust et al., 2004). In that sense, if the magma does not adequately release and expel volatiles as they are exsolving during magma ascent, the explosive potential of the system increases (Eichelberger et al., 1986).

Exsolving volatiles in silicic magmas like rhyolites, trachytes, and dacites usually gather in bubbles. Still, the high viscosity of these magmas inhibits bubbles from merging and migrating through buoyancy-driven fluid flow (Sparks, 2003). Crystallization past a critical packing fraction will also restrict bubble expansion and inhibit bubble migration (Oppenheimer et al., 2015). Inhibited bubble merging and migration while pore pressure increases within the bubbles can lead to bulk magma fragmentation, and ultimately, cataclysmic eruptions (e.g. Alidibirov and Dingwell, 1996; Papale, 1999). However, permeable networks can develop within silicic magma that provide escape for

\* Corresponding author at: Department of Earth Sciences, Uppsala University, Uppsala, Sweden.  
E-mail address: [steffi.burchardt@geo.uu.se](mailto:steffi.burchardt@geo.uu.se) (S. Burchardt).

pressurized exsolved volatiles, through bubble coalescence (Giachetti et al., 2019; Okumura et al., 2009) or fracturing (Heap et al., 2019; Kushnir et al., 2017; Okumura et al., 2010; Shields et al., 2014). Bubble coalescence and fracturing are two end members of outgassing mechanisms that are reached when viscosity and strain rates are either low enough for bubble coalescence, or high enough for the magma to fracture. In this study, we investigate the transition from bubble coalescence to fracturing, preserved in a solidified rhyolite intrusion.

Magma fracturing is a phenomenon known to take place extensively in the eruptive conduit and sub-volcanic environment of intermediate to silicic volcanoes (Benson et al., 2012; Gonnermann and Manga, 2003; Kushnir et al., 2017; Lamur et al., 2019; Lavallée et al., 2008; Tuffen et al., 2008). Tuffisites are remnants of the fracturing process, typically found along the edges of eruptive conduits both in the magma and extending outward into the host rock (Heap et al., 2019; Heiken et al., 1988; Unwin et al., 2021). Tuffisites testify to brittle deformation-driven outgassing of magma under high strain rates. However, outgassing is restricted to the surface area of the magma fracture (Castro et al., 2012; Heap et al., 2019), and therefore the bubbles within a large volume of the ascending magma remain pressurized.

In this study, we explore both viscous and brittle processes within a shallow rhyolite intrusion that are not localized to the host rock contacts. These deformation processes left traces within the bulk of the intrusion, which we describe and compare to published experimental works that contain identical textures to those in the natural setting of this study. We compiled these textural interpretations and present a model for deformation accommodating magmatic volatile transport throughout the magma volume, not just the host rock contacts. Detailed field observations and the broader context of shallow magma emplacement are addressed in the companion article (Witcher et al., 2024). Together both articles aim to shed light on permeability development within a shallow crustal silicic magma intrusion, allowing for pressurized magmatic volatiles to move through and exit the magma without erupting.

Here we focus on the microstructural analysis of the deformation features observed at the Sandfell laccolith in Eastern Iceland (Fig. 1). Specifically, we explore how the observed types of permeability formed and what rheological state the magma was in at the time. We then discuss different degassing and outgassing mechanisms for silicic magmas and their role for volcanic hazards.

### 1.1. Rheology

The mechanical behavior of magma is dictated by the contribution of its three components: solid crystals, gas-filled bubbles, and liquid silicate melt. Silicate melt rheology has been studied at length (Alidibirov and Dingwell, 1996; Dingwell and Webb, 1989; Hess and Dingwell, 1996; Webb and Dingwell, 1990), showing that silicate melt is a strain rate-dependent viscoelastic liquid: at low strain rates silicate melt flows viscously, but locks up and fractures like a solid when its relaxation time is exceeded by a critical deformation timescale (Dingwell, 1996; Wadsworth et al., 2018). Viscosity controls the relaxation time, and is in turn controlled by temperature and silica content as well as the magma's crystal and volatile content (Cordonnier et al., 2012; Giordano et al., 2004; Hess et al., 2001; Lejeune et al., 1999; Okumura et al., 2016). While an increase in crystals generally raises the magma's viscosity (Okumura et al., 2016), an increase in dissolved volatiles decreases the viscosity (Hess and Dingwell, 1996). For this reason, silica-rich magmas (like rhyolite, dacite, and trachytes) and crystal-rich magmas are driven towards viscoelastic behavior and brittle failure at lower stresses compared to silica-poor and crystal-poor magmas (Cordonnier et al., 2012). The presence of bubbles in suspension affects magma rheology depending on the gas volume fraction, but more on bubble shape (Birnbaum et al., 2021; Llewellyn et al., 2002; Mader et al., 2013; Rust et al., 2003). In general, bulk viscosity decreases with increasing bubble fraction except when surface tension forces are dominating and keep the

bubble in a relaxed spherical shape, whereby it behaves as a rigid particle (Llewellyn et al., 2002; Rust and Manga, 2002).

Magmas proportionally rich in crystals (55–70 %) are referred to as 'crystal mush', and have been suggested as the typical state of magma stored in the Earth's crust (Marsh, 2004; Sparks et al., 2019a). How the crystal mush behaves is under investigation, particularly its physical properties in order to better seismically image mush (Parmigiani et al., 2014; Paulatto et al., 2022; Sparks et al., 2019b), and determine how melt can travel through mush deeper in the Earth's crust (Holness, 2018; Katz et al., 2006; Pistone et al., 2015; Van Der Molen and Paterson, 1979; Walte et al., 2011; Zimmerman and Kohlstedt, 2004). Mush has been compared to a granular material containing a high volume fraction of solid particles (Zorn et al., 2020). Mush erupted at the Earth's surface in the form of lava domes (Allan et al., 2017; de Silva, 1989; Holness and Bunbury, 2006; Tait, 1988), as well as remnants of mushes in intrusions exposed at the surface (Marsh, 2004; Petford et al., 2020), have provided textural insights that have helped constrain mush dynamic theories. Numerical modeling (Carrara et al., 2024; Katz et al., 2006) and deformation experiments on the other hand (Holtzman et al., 2003; Kohlstedt et al., 2010; Pistone et al., 2015; Shields et al., 2014) have begun to disentangle the melt-migration behavior of mush in the deep crust and degassing/outgassing mechanisms of mush at shallower crustal levels. Together, studies of mush-derived rocks, models, and experiments highlight that as magma crystallizes and changes from a melt-dominated material to a crystal mush, its rheology changes—that is, its bulk response to applied shear (Dingwell and Webb, 1989). Increasing crystal fraction inhibits viscous flow, especially once there are more solid crystals than liquid melt (Champallier et al., 2008; Cordonnier et al., 2012). If the magma is continuously sheared during crystallization, deformation features will change depending on the crystallinity of the magma. Microscopic porosity among crystals within deformation features serve as tracers of the magma's changing rheology during deformation.

However, there is a general lack of observations of crystal mush behavior between the eruptive environment and deep storage zones. This is where more observations of crystal-rich magma are needed, particularly with respect to outgassing mechanisms. Such observations will also be useful to further constrain experimental results in natural and synthetic materials. Here we use micro-textural analyses to describe a range of magma-deformation features formed during the emplacement of a shallow rhyolite intrusion, interpret them based on results from experimental studies, and discuss the implications for magma rheology, degassing, and outgassing.

### 2. Geological setting and previous work

Iceland straddles the mid-Atlantic spreading center, and is rifting towards the NNW and SSE at an average rate of 2 cm/yr within its rift zones (Fig. 1a, inset) (Sigmundsson et al., 2020). The rifting orientation has been generally consistent for the last ~20 Ma (Martin et al., 2011) and, as a result, the oldest rocks in Iceland are preserved on the eastern and far-western coasts (Burchardt et al., 2022). Eastern Iceland is punctuated by large volcanic complexes that consist of a central volcano, its eruptive deposits, and various associated intrusions like dykes, sills, and laccoliths (Burchardt et al., 2022; Walker, 1974). Generally, silicic magmatism is restricted to the central volcanoes (Walker, 1966).

The Sandfell laccolith lies in the south end of Fáskruðsfjörður, Eastern Iceland, and is a cryptodome of the extinct Reydarfjördur central volcano (Gibson, 1963; Hawkes and Hawkes, 1933). Field mapping concluded that the timing of the laccolith's intrusion was during the fourth eruptive phase of the Reydarfjördur volcano (Gibson et al., 1966) and recent U–Pb dating of zircons identified an absolute age of Sandfell of 11.7 Ma (Martin and Sigmarsdóttir, 2010; Padilla et al., 2015). The Sandfell laccolith consists of a fine-grained, phenocryst-poor (<5 % sub-mm sized plagioclase) rhyolite with a silica content of 74 wt% (Martin and Sigmarsdóttir, 2010). Despite the uniform composition, several

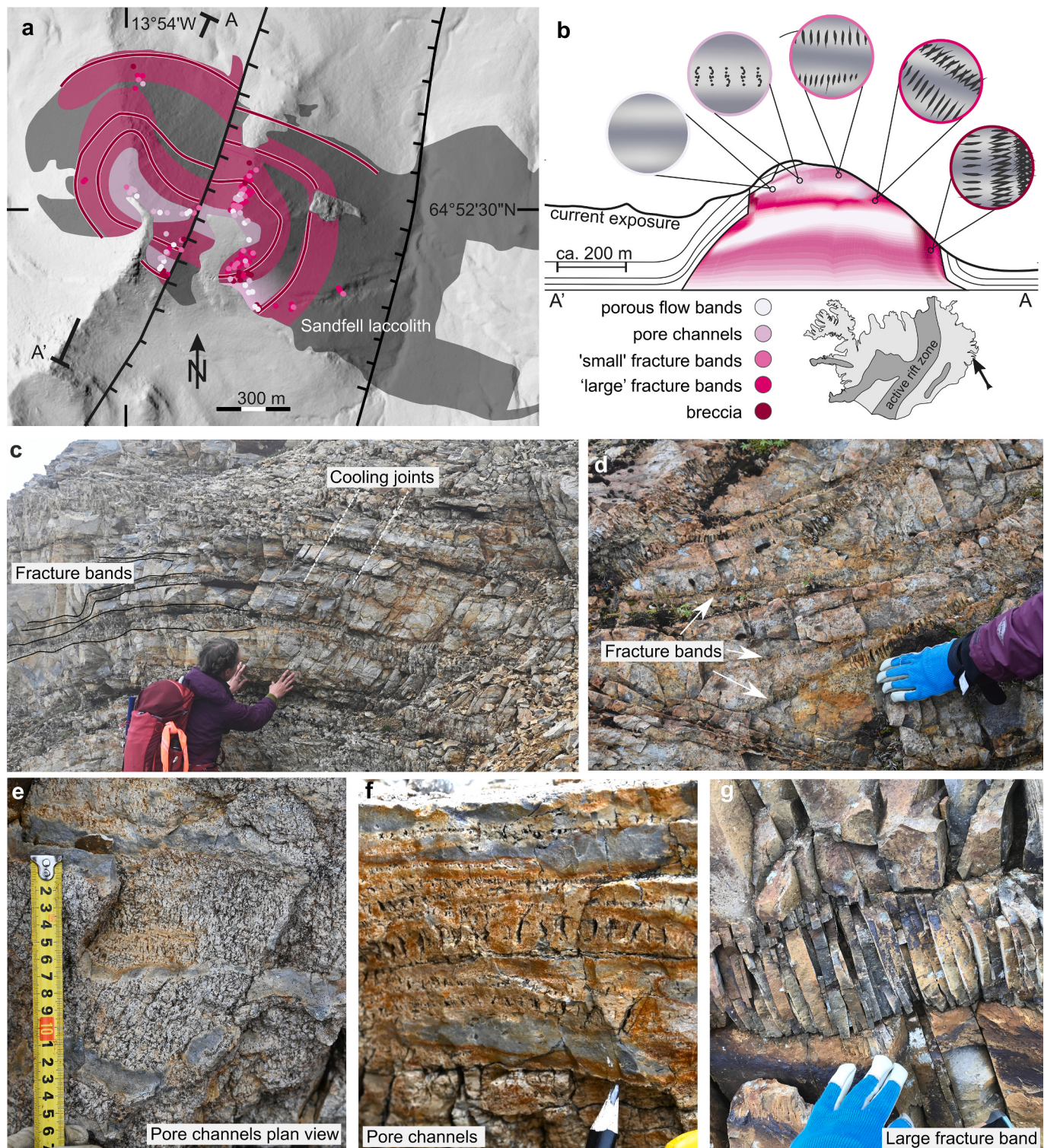


**Fig. 1.** Location and photographs of the Sandfell laccolith, modified from Witcher et al. (2024). a) Map view of the entire laccolith, the regional location indicated with an arrow in inset. Structural domains indicated in pink, defined by the mapped distribution of deformation marked with dots, scale found in b). Light-shaded areas have more viscous deformation, dark-shaded areas have more brittle deformation. Bands within dark areas are interpreted to represent emplacement-related faults. b) Schematic cross section of A-A' showing the large-scale strain localization recorded by the different deformation types (schematic drawings in circles; see Table 1 for details). c & d) Outcrop photos of fracture bands and cooling joints. e) & f) Example of pore channels in the exposed plane (e) and cross-section (f). g) Cross-sectional exposure of a large fracture band. (For interpretation of the references to color in this figure legend, the reader is referred to the web version of this article).

interior structural domains with a unique deformation history could be identified within the main body of the laccolith, suggesting the laccolith was constructed through the amalgamation of several pulses of magma (Fig. 1a & b) (Witcher et al., 2024).

Mattsson et al. (2018) were the first to report on the remarkable fracture network preserved in the Sandfell laccolith: bands of dominantly tensile, uniformly spaced fractures are preserved in outcrop, termed ‘fracture bands’ (Fig. 1c & d). Fracture bands are concentrically stacked between layers of coherent (unfractured) rhyolite, and range in thickness from cm- to dm-scale. The length of fracture bands varies; sometimes they pinch out in less than one meter, sometimes they span meters in a planar fashion, and other times they undulate and join neighboring fracture bands, thickening and overtaking the coherent magma layers such that there is more fractured than coherent rock in a single outcrop.

Mattsson et al. (2018) concluded the fractures formed in the magmatic state and were caused by inflation-related stresses. They qualitatively attributed the preservation of the fractures in outcrop to the dehydration of fractured melt upon fracture formation. Further, they noted concentrated vesicles in the fracture bands compared to unfractured rhyolite at outcrop scale, implying the fractures played a role in magma degassing. Based on detailed investigation of the fracture bands and other features, such as flow bands and bubbles in Sandfell, Witcher et al. (2024) identified the following mesoscale structures in outcrop and hand samples: 1) flow banding with alternating bands of porous and non-porous rhyolite, 2) vertically aligned pores within flow bands, termed ‘pore channels’, 3) “small” fracture bands, 4) “large” fracture bands, and 5) breccia (Table 1). It is the distribution of these deformation features that outlines the different structural domains (Fig. 1a & b; Witcher et al., 2024). Here, we focus on the corresponding microstructures to investigate the origin and implications for magma degassing and outgassing.

In this study, we define a *pore* as a discrete void within the material. The types of porosity will be described using the following terms: *bubble*, a spherical pore formed by the expansion of gas within a liquid (undeformed aspect ratio between length  $l$  and width  $w$ :  $l/w = 1$ ); *vesicle*, a preserved bubble within rock (smooth walls, ellipsoidal shape,  $l/w \approx 1$ ); and *fracture*, the result of mechanical failure through dominantly brittle

deformation (planar, jigsaw-fit walls,  $l/w \gg 1$ ). If a pore type does not fall under the category of vesicle or fracture, it is referred to simply as a ‘pore’.

### 3. Methods

We employ the following methods to closely investigate 1) the range of pore geometries, and 2) the properties of the magma at the time of pore formation. Samples were collected from the field during campaigns in 2018, 2019, and 2021. Given that analytical sample preparation was only feasible on rocks recording deformation stages 1–3, in this study, we focus on flow bands, pore channels, and small fracture bands. A summary of the methods and the motivation for each method can be found in Table 2.

We prepared thin sections and first used optical petrography to analyze pore geometry. We then turned to scanning electron microscopy (SEM) to investigate fracture and pore geometry, mineralogy, and groundmass deformation in more detail. We took porosity and permeability measurements of flow-banded samples, measuring permeability parallel and perpendicular to the flow band plane to quantify any preference of fluid flow. To characterize the connection of fractures within fracture bands, we employed micro-computed tomography ( $\mu$ CT) and scanned fracture band samples in 3D. The mineralogy of fracture fillings and rhyolite groundmass was identified with the electron microprobe (EMP) and Raman spectroscopy, as well as Ti-content in quartz for geothermometry. We describe each method in more detail below.

#### 3.1. Thin section microscopy

Standard polished thin sections were prepared at Precision Petrographics laboratories in Langley, Canada, and ERZ Labor in Freiberg, Germany. Blue epoxy was used in some thin sections to highlight porosity. The thin sections were observed and described using transmitted light and scanning electron microscopy (SEM).

**Table 1**

Range of deformation features found in outcrop at the Sandfell laccolith, and their defining characteristics. Fracture bands (large) and breccia are excluded from this study, but present in outcrop and described in more detail in Witcher et al. (2024).

Feature name:	Defining characteristics in hand sample:	Figure reference:
Porous flow bands	<ul style="list-style-type: none"> <li>Parallel bands of mm-thickness</li> <li>Tan color against grey rhyolite</li> <li>Visibly more porous, both in cross section and when the flow band plane is exposed</li> <li>Vertically elongated pores within the flow band</li> </ul>	Fig. 2b
Pore channels	<ul style="list-style-type: none"> <li>Oriented perpendicular to flow band plane</li> <li>Tensile in appearance: widest at center and pinch out at tips</li> <li>Shape controlled by flow band thickness</li> <li>Sharp, planar fractures of cm- to dm-thickness</li> </ul>	Fig. 1e, f Fig. 2c
Fracture bands	<ul style="list-style-type: none"> <li>Oriented perpendicular to the band they form</li> <li>Uniform size and spacing</li> <li>&lt;5 cm thick and/or 1 fracture set</li> </ul> <p>Not described in this study, but present at the Sandfell laccolith:</p>	Fig. 1c, d, g Fig. 2d, e
Fracture bands (large)	Same appearance as fracture bands, only larger; ≥5 cm thick and/or > 1 fracture set within single band	Fig. 2f
Breccia	Indistinguishable bands with similarly oriented fractures, or complete cataclasite	N/A

**Table 2**  
List of methods and research questions to be addressed by each method.

Method	Research question addressed by method	Results:
Optical petrography	Is there a difference in magmatic texture inside vs outside the fracture band? How are pores interacting with crystals?	Sec. 4.1
SEM imaging	What does the groundmass texture look like? What do the pore walls and tips look like?	Sec. 4.1
FOAMS	How do the size distributions of flow band pores & pore channels compare?	Sec. 4.3
vesicle analysis	Can we quantify the difference in pore shape between textures?	
EMP (mineral ID)	What is the groundmass mineralogy?	Sec. 4.2
Raman spectroscopy	Is there interstitial glass between microlites? Is the silica within pores cristobalite (vapor-deposited)?	Sec. 4.2 Is there a difference between groundmass and pore-filling silica?
CL imaging	Are the silica crystals zoned?	
EMP (Ti-in-quartz)	At what temperature did the silica crystallize?	
Porosity & permeability	Is the undeformed rhyolite permeable?	Sec. 4.1
$\mu$ CT scans	Are the flow bands permeable? How do the fracture bands look in 3D? How connected are the fractures within a fracture band?	Sec. 4.1

### 3.2. Scanning electron microscopy (SEM) and electron microprobe analysis (EMPA)

We used a FE-EPMA Jeol JXA-8530F Hyperprobe at Uppsala University, Sweden, to take backscattered electron (BSE) images, and to measure relative element abundance through energy dispersion spectroscopy (EDS) point analyses. Settings of the EMP and analytical standards are described in more detail in (Barker et al., 2015). Wavelength dispersive spectroscopy (WDS) measured the chemical composition with a 5–10  $\mu\text{m}$  electron beam. BSE images have a resolution of 1280  $\times$  960 pixels. Analysis of the acquired BSE images was performed in ImageJ FIJI, thresholding different greyscale values to highlight the silica grains.

BSE images were also segmented using the Weka tool (Arganda-Carreras et al., 2017) to isolate pores with an area greater than 0.001  $\text{mm}^2$  (at 0.44  $\mu\text{m}/\text{pixel}$ ) for shape analysis, and pores with more than 20 pixels for size distribution plots following Marsh (1988), substituting pores for crystals. Pore shape properties were analyzed using the FOAMS software from Shea et al. (2010) to get vesicle size distribution (VSD). Equivalent object size fractions (L) are defined as the diameter of a sphere equivalent to the long axis of the pore. We assumed spherical shapes of the pore channels to account for their larger size than the pores within porous flow bands. The pore channels' elongation is accounted for in volume fraction size distributions, where elongation is defined as  $\varepsilon = (a - b)/(a + b)$ , where  $a$  is best-fit ellipse semi-long axis and  $b$  is semi-short axis. Elongation  $\varepsilon = 0$  means perfectly circular and  $\varepsilon = 1$  means extremely elongated (Shea et al., 2010). We analyzed two data sets comprised of even- and odd-numbered BSE images, since there was overlap of the images in sequence. The closeness of the resulting curves shows the consistency of the analyses.

To give an approximation of the crystallization temperature of quartz within the Sandfell rhyolite fractures and groundmass, we performed WDS measurements of Ti in quartz on 30  $\mu\text{m}$ -thick polished thin sections with a 25 nm-thick carbon coating. Measurements were performed with a Jeol JXA-iSP100 electron probe micro-analyzer at the University of St. Andrews, Scotland, with a beam radius of 15  $\mu\text{m}$ , peak counting times of 200 s and background counting times of 100 s. Measurements were run at 20 kV acceleration voltage and a beam current of 70 nA. Therefore, only large quartz crystals and phenocrysts could be analyzed for Ti content. Ti detection limit for the measurements was 13 ppm with a measurement error ( $1\sigma$ ) ranging up to 50 % ( $\pm 6.5$  ppm). Eight quartz crystals were analyzed for Ti content with a total of 36 measurements. We used the average Ti content of all the measurements for the Ti-in-quartz geothermometer following Wark and Watson (2006). A  $\text{TiO}_2$  activity value of 0.7 was applied, following thermodynamic modeling in felsic magmas (Carter et al., 2021; Ghorso and Gualda, 2013). Monochromatic Cathodoluminescence (CL) images of quartz crystals in the groundmass and pores were taken with the JEOL JXA isp-100 EMPA operated at 15 kV accelerating voltage with an attached CLi detector in 5120  $\times$  3840 resolution. Brightness and contrast were optimized to distinguish internal features within silica crystals.

### 3.3. Microcomputed tomography ( $\mu\text{CT}$ )

The thin section slabs were scanned at Delft University of Technology (the Netherlands) using a Phoenix Nanotom X-ray micro-tomograph (model 180NF), with a beam energy of 180 kV and a resolution of 22.5  $\mu\text{m}/\text{voxel}$ . Using Avizo  $\circledcirc$  software (version 10) all scans were processed to segment pore volume and fracture fill material versus groundmass. In the scans used for this study, the quality was sufficient to use thresholding without any data filters. Three segmentation categories were used, where the rest was attributed the label of 'matrix'. The fracture-filling material could be separated between high intensity (i.e. high density) material and medium intensity material, versus open space (i.e. dark voxels). After each thresholding step, small ( $>50$ – $500$  voxels; size chosen depending on the results of each segmentation) clusters of

isolated voxels ('islands') were removed. Once the segmentation was completed to satisfaction, we created the colorized scans where nearby connected voxel clusters have the same color, and retrieved volumes associated with each thresholding category.

### 3.4. Raman spectroscopy

We determined the polymorph of silica present in the groundmass and pores of the rhyolite by using Raman spectroscopy on selected grains in polished thin sections. The Raman scattering experiments were performed at the Department of Earth Sciences, Uppsala University, using a self-built micro-Raman system. The DPSS laser (Cobolt Samba, 532.42 nm) was used as the excitation source in the backscattering geometry. The laser beam was focused down to a spot size of  $\sim 2$ – $4$   $\mu\text{m}$  on the sample surface by a 20 $\times$  long-working distance objective (Nikon CF Plan, 20 $\times$ /0.35). The Rayleigh line was blocked by two holographic notch filters (Semrock). A single-stage, high-throughput imaging spectrometer (HoloSpec f/1.8i, Kaiser Optical Systems, Inc.) was used to analyze the scattered light, collected by the CCD detector (Newton, Andor Technology, 1600  $\times$  400 pixels, TE-cooled to  $-55^\circ\text{C}$ ). The system was calibrated using fluorescence lines of a neon lamp. The spectral resolution of the system was around 4  $\text{cm}^{-1}$  and the accuracy estimated from the calibration procedure was around 2  $\text{cm}^{-1}$ . The Raman spectra were collected in the range 150–1700  $\text{cm}^{-1}$  at room temperature, applying 10 mW of the laser power. The spectral acquisition time varied between 30 and 120 s.

### 3.5. Porosity & permeability measurements

Cores with 1-cm diameter were drilled parallel and perpendicular to flow bands. The samples were first vacuum-dried at 40  $^\circ\text{C}$  for at least 48 h. The connected porosity of each sample was then calculated using the skeletal volume measured by a helium pycnometer (AccuPyc II from Micromeritics) and the bulk sample volume was measured using digital callipers. Permeability was measured for each sample using a benchtop gas (nitrogen) permeameter (see Farquharson et al., 2016; Heap and Kennedy, 2016) for a schematic diagram of the device). Permeability measurements were performed at ambient temperature and under a confining pressure of 1 MPa using either the steady-state method (for high-permeability samples) or the pulse-decay method (for low-permeability samples). For the steady-state experiments, steady-state volumetric flow rates were measured (using a gas flowmeter) for six different pore pressure differentials (measured using a pressure transducer). Pulse-decay measurements were performed by monitoring the decay of a pressure differential from an upstream reservoir with a fixed volume over time (measured using a pressure transducer). These data were used to calculate permeability using Darcy's law (all the relevant equations can be found in Heap et al., 2017). When necessary, the data were corrected using the Klinkenberg or Forchheimer corrections.

## 4. Results

### 4.1. Rhyolite textures

As shown by Witcher et al. (2024), the top 140 m of the Sandfell laccolith consists of four units representing successively emplaced magma batches. These magma batches do not differ in composition, and all of them exhibit magmatic flow banding. Witcher et al. (2024) demonstrated that flow banding resulted from strain during magma emplacement, based on detailed analyses of the orientation of flow banding. While the different deformation features (Table 1) show a complex distribution pattern related to the emplacement of the Sandfell laccolith (Fig. 1; Witcher et al., 2024) and distinct textural characteristics, the groundmass remains mostly consistent (Fig. 2). The groundmass is largely composed of euhedral alkali feldspar microlites (<20  $\mu\text{m}$  long) (Fig. 2a) with interspersed poikilitic quartz aggregates, identified

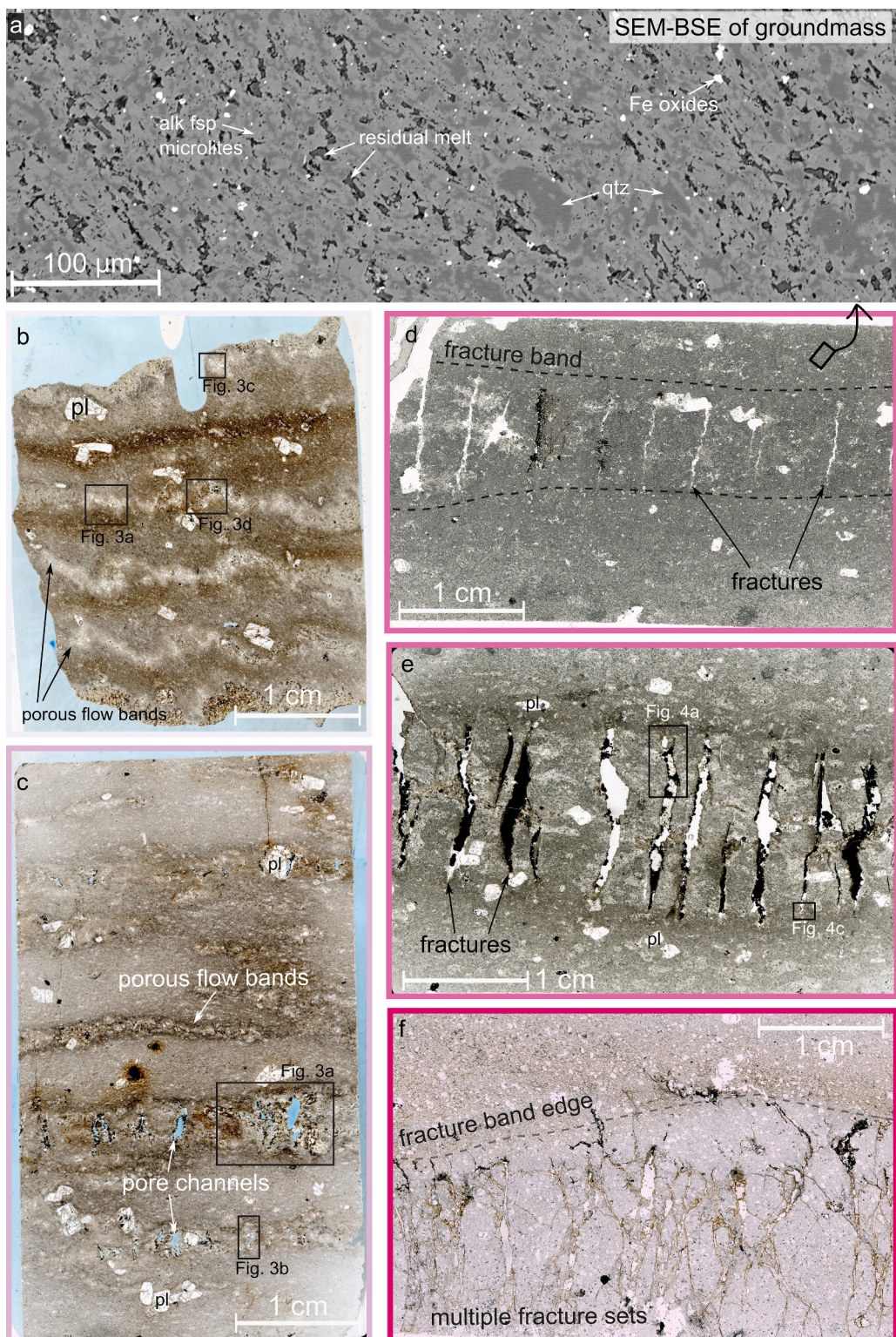


**Fig. 2.** Back-scattered electron (BSE) image of groundmass (a) and thin section scans representing each deformation stage (b-f). Short axis of thin sections is ca. 2.5 cm. See color scale of the frames in Fig. 1b). a) BSE image of groundmass. Quartz grains are mid-grey (labelled), microlites are light grey, mafic oxides are white and residual melt is the dark grey phase between microlites. b) Flow banded rhyolite; flow bands defined by higher vesicularity. pl = plagioclase phenocrysts. Dark staining is from Fe-rich weathering. c) Pore channels; elongated pores oriented perpendicular to flow band, aligned with some regularity. Blue epoxy highlights empty space. d) Fracture band example; band of tensile fractures uniform in length, width, and spacing. No visible change in groundmass texture at this scale. e) Fracture band example; larger band containing more widely open fractures with mineral fillings. Dark material is Fe-rich oxides. f) Example of fracture band containing multiple fracture sets, indicating it would be classified as a ‘large’ fracture band (Table 1). (For interpretation of the references to color in this figure legend, the reader is referred to the web version of this article.)

with Raman spectroscopy as  $\alpha$ -quartz (Supp. Mat. 1). These quartz aggregates are termed ‘groundmass quartz’ when they are lined with microlites, and ‘pore-filling quartz’ when they are euhedral within a pore. Quartz aggregates occur preferentially in porous flow bands, flow bands with pore channels, and fracture bands. Microlites are often fractured and encased in the groundmass quartz (Fig. 2a). Quartz (with or without microlite inclusions) is rarely fractured. Small ( $\sim 10 \mu\text{m}$ )

euhedral titanomagnetite crystals occur throughout the groundmass. Filling the remaining space between microlites is a phase with a darker greyscale on the BSE image than quartz. This phase is often fractured into polyhedrons (similar to mud cracks; Fig. 2a) and interpreted to be a vitreous material that was once residual melt; no quantifiable measurements could be taken due to exposures being less than 5–10  $\mu\text{m}$ , which was the diameter of the electron beam. Millimeter-scale,

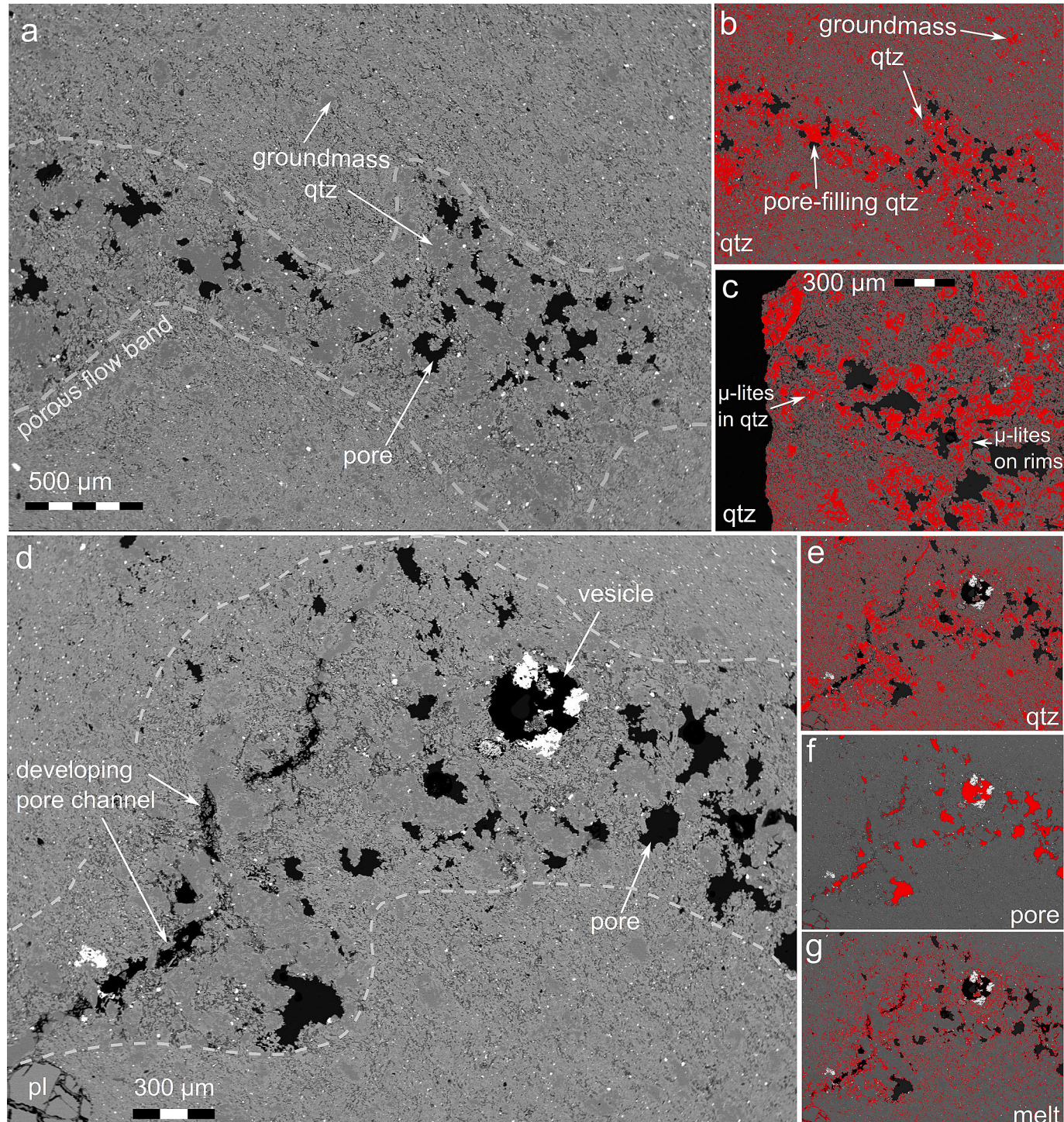


**Fig. 3.** BSE images of porous flow bands (see Fig. 2b for locations), and thresholded images highlighting different phases in red. a) Porous flow band, outlined with dashed lines. Black is void space, mid-grey is quartz, light grey is alkali feldspar microlites, and white is Fe-rich oxides. b) Same image as a) with quartz highlighted in red. c) Quartz-thresholded image of a porous flow band with microlite inclusions in the quartz between porosity in the flow band. d) Porous flow band with a vesicle and developing pore channel. Same color scale as a). pl = plagioclase phenocryst. e-g) Thresholded images of (d) highlighting quartz, pores, and vitreous material (melt) phases. (For interpretation of the references to color in this figure legend, the reader is referred to the web version of this article.)

commonly broken euhedral to subhedral plagioclase phenocrysts make up ~5 vol% of the rhyolite.

Porous flow bands (Fig. 2b) are defined as bands with high porosity with respect to the coherent rhyolite layers in between them (see Section 4.1.1). Pore channels refer to the elongate pores that are confined and oriented sub-perpendicular to the flow bands (Fig. 2c; see Section 4.1.2). Within fracture bands, fractures range in thickness from 1 to 25 cm (Fig. 2d, e; 1c, d, g; see Section 4.1.3). The size of the fractures does not appear to correlate with the presence of mineral fillings: while smaller fractures tend to contain no or little fracture fillings (Fig. 2d), larger fractures adjacent to each other can range from filled to entirely open (Fig. 2e). Generally, the fractures are confined to the flow bands and do not extend into the surrounding, coherent layers of rhyolite (Fig. 2d-f). The surrounding groundmass tends to not vary between the fracture bands (Fig. 2c), but fracture bands may be bounded by a darker rim within the groundmass along the upper and lower boundaries of the fracture band (Fig. 2d). In the following sub-sections, we will describe the textures associated with each of these deformation features.

#### 4.1.1. Porous flow bands

BSE imaging of the flow bands highlights alternating layers characterized by changes in porosity (in black in Fig. 3), as well as the concentration and size of aggregates of poikilitic quartz grains (in red in Fig. 3b, c & e). Area calculations on thresholded images (Fig. 3) resulted in quartz making up ~28 % of the area within porous flow bands, compared to ~15 % of the area in the surrounding groundmass (Fig. 3). In the porous flow bands, large pores (~100 µm) occur between the quartz grains and exhibit sub-circular to irregular geometries (Fig. 3). Microcrystals are commonly encased within the groundmass quartz aggregates and almost always line the margins of quartz grains within the porous flow bands (Fig. 3a-c). In contrast, the ‘pore-filling quartz’ is free of microlites (Fig. 3b). Microporosity (<10 µm) is dispersed

throughout the porous flow band between microlites, as well as the vitreous material interpreted as interstitial melt (Fig. 3d, lower right panel). Some segments of a porous flow band have less porosity in the form of smaller or fewer pores. Rare circular vesicles with smooth edges occur within the porous flow bands (e.g., Fig. 3d). The vesicle shape is in contrast to that of elongated pores that avoid quartz aggregates (Fig. 3d).

#### 4.1.2. Pore channels

Pores that are elongated and oriented roughly perpendicular to flow banding are classified as pore channels (Fig. 4; 2c). Pore channels typically have much larger pores (100–1000 µm along the longest axis) than porous flow bands (Fig. 4a; 2). Euhedral ‘pore-filling quartz’ (as described in Section 4.1.1; Fig. 4b & c; Supp. Mat. 2) occurs more frequently within the pore channels compared to the porous flow bands (e.g. Fig. 4a-c; 5b & c). Area calculations on thresholded images (Fig. 4) resulted in quartz making up ~22 % of the area within the pore channel flow band as compared to ~13 % of the area in the surrounding groundmass. Between the large, elongated pores in the pore channels, microporosity resembles the textures described for porous flow bands (Fig. 4a & b; compare Section 4.1.1 and Fig. 3) with prevalent diktytaxitic texture (Fig. 4d). The vitreous material (melt) between microlites is observed to host fragments of various mineral clasts, e.g. inside a ~50 µm pore (Fig. 4e). Along with the clast fragments are variably deformed vesicles near the margin towards the microlites (indicated by the red arrows in Fig. 4e & f).

#### 4.1.3. Fracture bands

Fractures within fracture bands have a dominantly brittle appearance (Fig. 2c & d), with high aspect ratios ( $l/w \gg 1$ ), and often *en echelon* configurations within the fracture band (Fig. 2e). In addition to their morphology, fractures are also significantly longer (>1 cm) than mm-

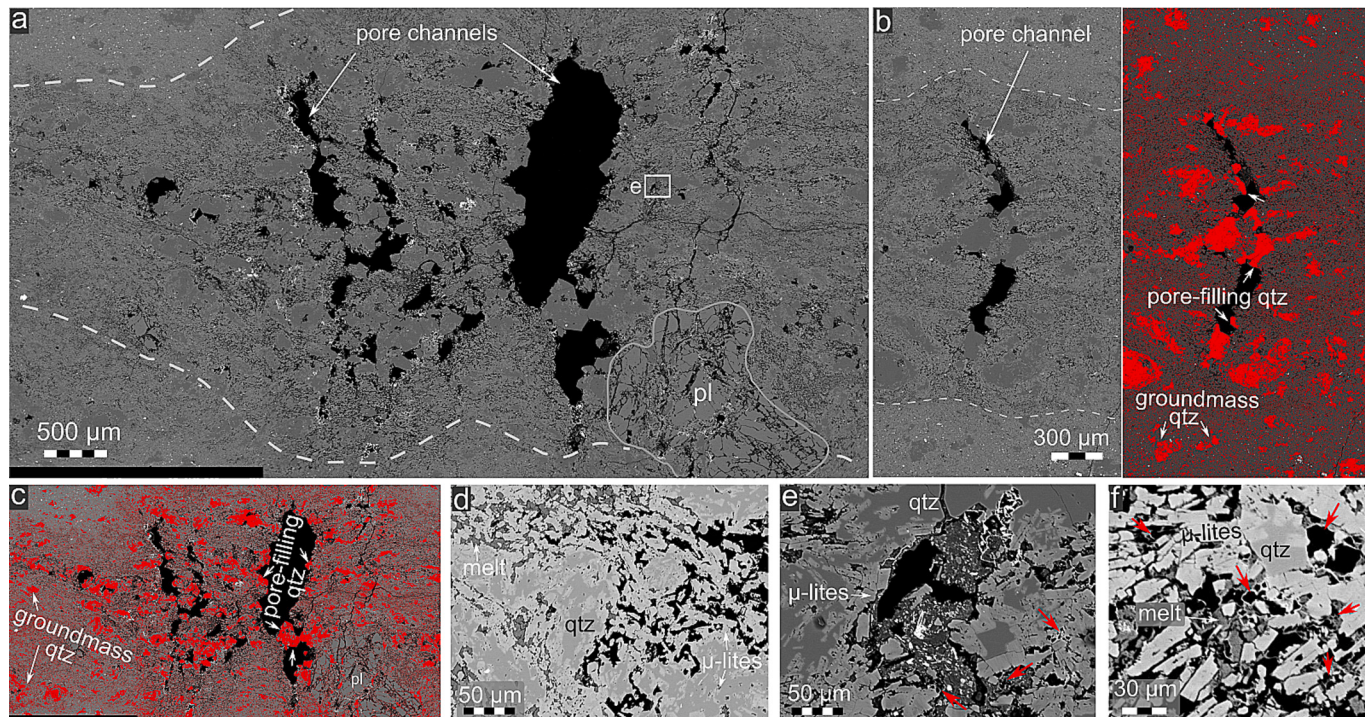


**Fig. 4.** BSE images of pore channels (see Fig. 2c for locations). a) Cluster of elongated pores, development of brittle fractures on the right. Black is void space, dark grey is interstitial melt, mid-greys are quartz and alkali feldspar microlites, and white is Fe-rich oxides. b) BSE and quartz-thresholded image of an elongated pore bisected by quartz grains rooted in the groundmass. Color scale is the same as in a). c) Same image as a) with quartz highlighted in red; microlite-rich groundmass quartz and microlite-free euhedral pore-filling quartz are labelled. d) Diktytaxitic texture in the groundmass. e) Close-up of groundmass and pores filled with broken clasts of oxides (white) and groundmass minerals suspended in melt, with red arrows pointing to deformed bubbles. f) Close-up of melt + microcryst texture, red arrows point to bubbles. (For interpretation of the references to color in this figure legend, the reader is referred to the web version of this article.)

scale pore channels and porous flow bands (Fig. 2). Like the pore channels, the long axis of the fractures is oriented perpendicular to flow-banded fabric of the groundmass (e.g. Fig. 2d & e).

No strong correlation is observed between size, shape, or distribution of quartz in the groundmass relative to fractures (Fig. 5a & b). Fracture tips are forked and grade into the groundmass rather than appearing

sharp or blunt (Fig. 5a - d). More specifically, fracture tips are seen to extend into the groundmass through channels filled with vitreous material (melt) that avoids the groundmass quartz (Fig. 5e & f, inset). *En echelon* configurations of fracture tips are common in the fractures (e.g. Fig. 5e & f). The vitreous phase is also found surrounding euhedral pore-filling quartz protruding into the fractures (Fig. 5g). Fracture walls can

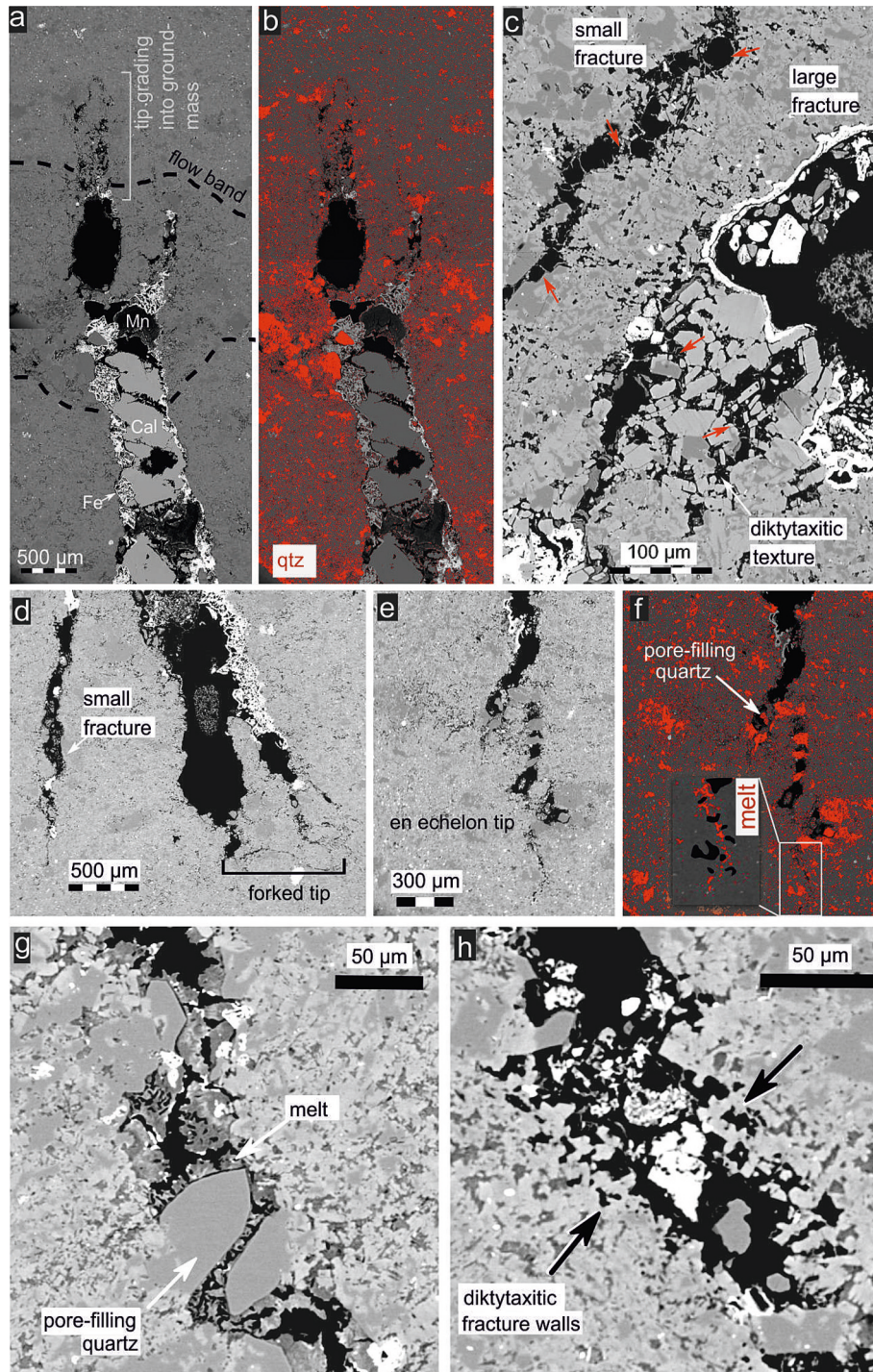


**Fig. 5.** BSE images of fractures within fracture bands, and thresholded images with quartz highlighted in red. Contrast has been enhanced to better visualize the groundmass. Black is void space, and white is Fe-rich oxides. a) Forked fracture tip grading into groundmass (see Fig. 2e for location). cal = calcite, Fe and Mn = iron- and manganese-rich phases. Flow band outlined with a dashed line. b) Same as image (a) thresholded to highlight quartz. c) Small and large fractures containing melt filaments resembling bubble walls (red arrows). d) Doubly-forked tip of large fracture (right), and smaller fracture (left). e) and f) Fracture tip (see Fig. 2e for location) showing *en echelon* steps, avoiding the quartz (highlighted in f). Inset shows melt phase thresholded, fracturing avoids quartz. g) Pore-filling quartz surrounded by the melt phase. h) Fracture walls showing diktytaxitic texture. (For interpretation of the references to color in this figure legend, the reader is referred to the web version of this article.)

be straight and smooth or gradational, similar to the tips, grading from open space, through diktytaxitic texture, and into microlites suspended in vitreous material (Fig. 5g & h). Smaller fractures occur next to larger ones (left fractures in Fig. 5c & d), exhibiting undulating and jigsaw-fit walls, and occasionally remnants of melt filaments that resemble bubble walls (red arrows in Fig. 5c).

#### 4.2. Mineral analysis

As mentioned in Section 4.1, Raman spectroscopy identified quartz in both the groundmass (Fig. 2a) and protruding into void space in pore channels and fractures (pore-filling quartz: Fig. 4; fractures: Fig. 5). We measured the Ti-content in quartz of both settings to estimate crystallization temperatures following Wark and Watson (2006). Both quartz types yielded temperatures of  $718 \pm 60$  °C (more details in Supp. Mat. 3). Importantly, crystallization temperatures and crystal structure of the groundmass and pore-filling quartz are identical.

CL images of quartz grains reveal compositional growth zones in the groundmass and pore-filling quartz (Fig. 6). Pore-filling quartz is variably zoned with no microlite inclusions in the bulk of the crystal, with an increasing number of microlite inclusions closer to the pore edge (Fig. 6a). Groundmass quartz contains microlite inclusions throughout the grain, with no preference to specific compositional zones (Fig. 6b).

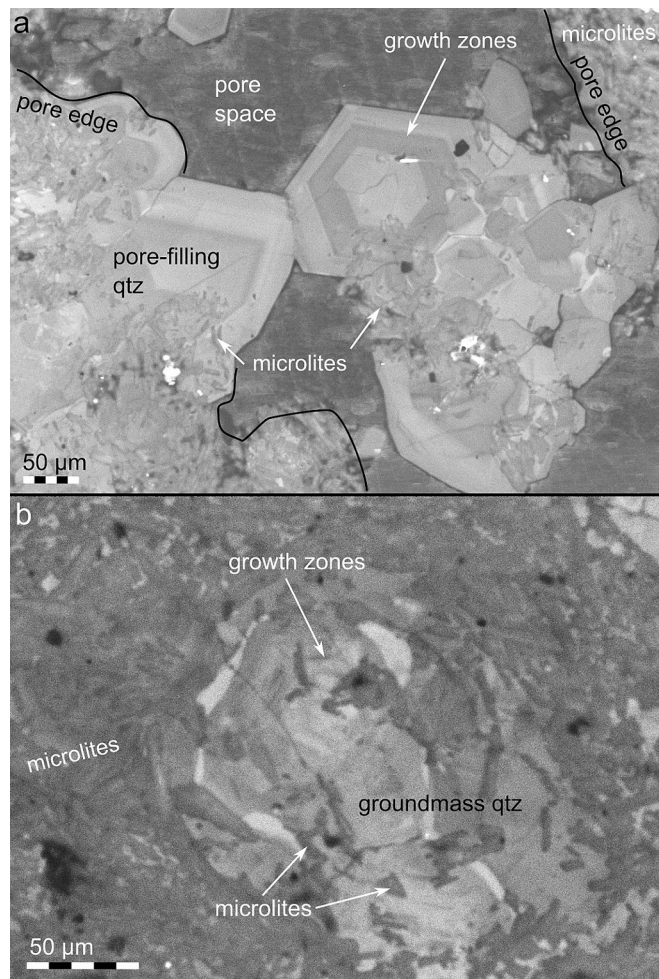


**Fig. 6.** Cathodoluminescence images of poikilitic pore-filling (a) and groundmass (b) quartz. Compositional growth zones and microlite inclusions are labelled.

#### 4.3. Porosity characterization

Cores prepared perpendicular to flow bands yielded connected porosity ( $\phi$ ) and permeability ( $k$ ) values of  $\phi = 0.08$  and  $k = 6.86 \times 10^{-18} \text{ m}^2$  (Fig. 7a), while cores prepared parallel to flow bands yielded  $\phi = 0.22$  and  $k = 2.05 \times 10^{-14} \text{ m}^2$  (Fig. 7b). Hence, there is a preference (by several orders of magnitude) for fluid flow aligned parallel to flow bands.

Vesicle size distribution (VSD), cumulative vesicle number densities (CVND), and pore shape analyses of porous flow bands and pore channels are plotted in Fig. 8. For porous flow bands, the VSD curves are convex after sizes of  $L = 0.12 \text{ mm}$ , whereas the VSD curves for pore channels are concave and reach higher  $L$  values (Fig. 8a). The CVND plot shows both flow band pores and pore channels decreasing in size linearly, before the flow band pores abruptly drop in number at size fractions  $\log(L) = -0.7$  (Fig. 8b). Volume fraction size distribution plots for flow bands (Fig. 8c) and pore channels (Fig. 8d) both show a Gaussian distribution, with a steep drop in  $\epsilon = 0.75$  among the pore channels (Fig. 8d).

$\mu$ CT imaging of fracture bands (Fig. 9) shows that fractures are significantly longer in the direction parallel to the opening (thickness) compared to the direction perpendicular to the opening (compare Fig. 9b & a). In both orientations the fractures terminate along a boundary invisible at this resolution/to this method. Individual fractures exhibit a 'stretched penny' shape, as well as higher porosity between fractures than in the unfractured groundmass (Fig. 9c). There is clearly a 'primary' fracture set that comprises the largest fractures in both length and aperture, separated by a 'secondary' fracture set that is smaller, and often oriented slightly oblique to the primary set (Fig. 9a & b). Fractures are variably filled with different minerals, as depicted by the range of greyscales within each fracture (Fig. 9a & b). No systematic pattern of mineralization was observed, and the fractures within this sample were calculated to be 80 % filled, with 20 % void space (Fig. 9d).

Through greyscale thresholding, we calculated the connectivity of each phase within the fractures. The results show that, at this scale, primary fractures are isolated from each other unless joined via

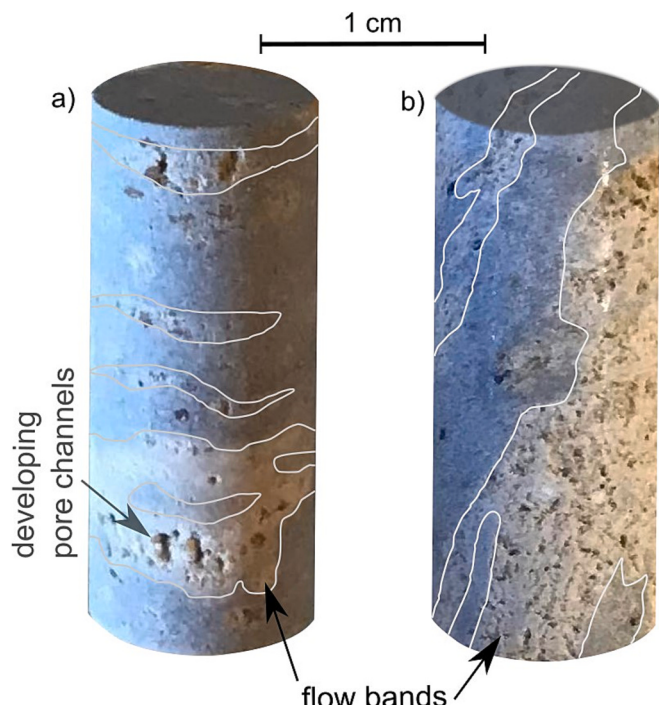


**Fig. 7.** Photographs of flow-banded cylindrical core samples, the porosity and permeability of which were measured a) perpendicular to flow banding and b) parallel to flow banding.

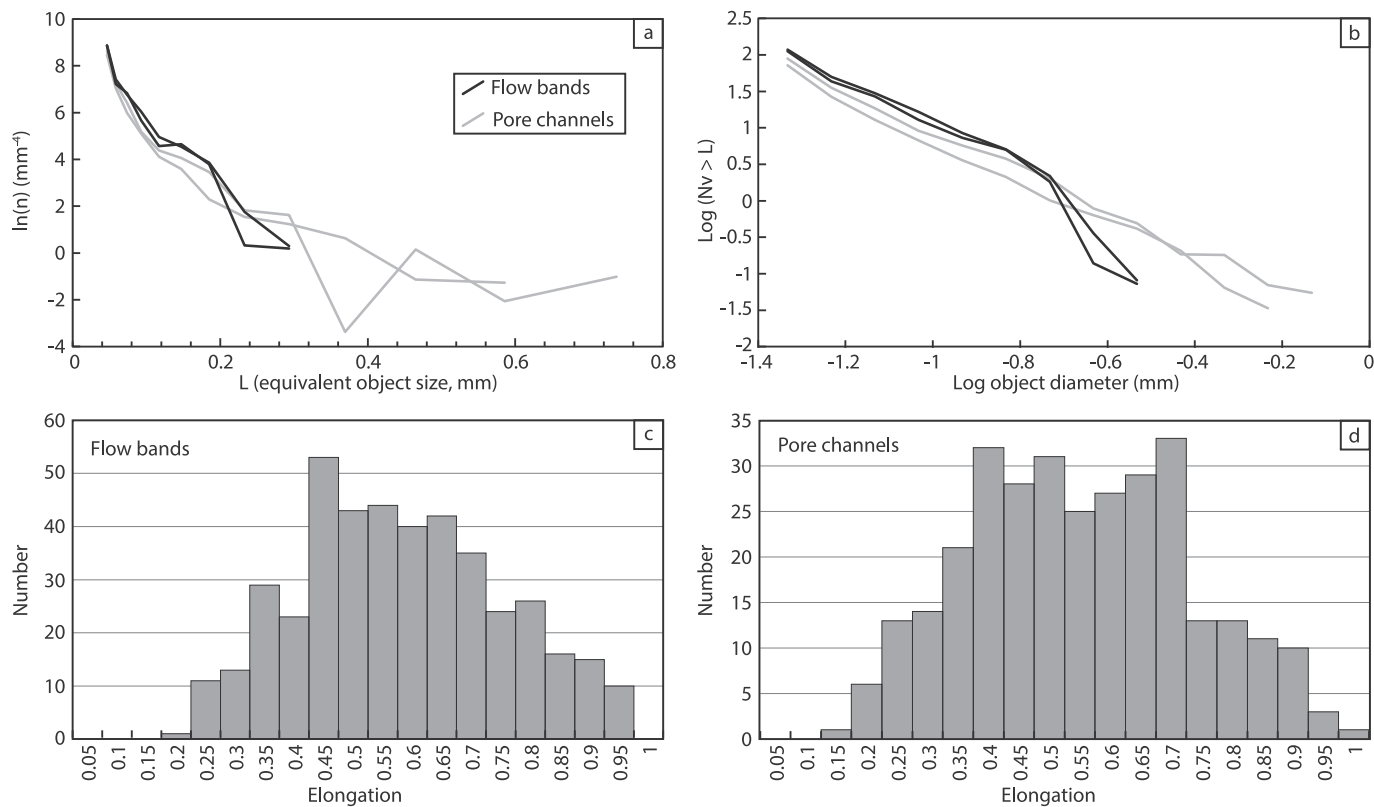


**Fig. 8.** Pore shape analysis plots for flow bands and pore channels following Shea et al. (2010). a) Vesicle size distribution (VSD) plot Number density ( $N_v$ ) against object size ( $L$ ). b) Cumulative vesicle number density (CVND) plot; Log number density of pores larger than 20  $\mu\text{m}$  against  $\log(L)$ . c) Volume fraction size distribution for flow bands ( $n = 425$ ) and (d) pore channels ( $n = 311$ ). Elongation parameter is such that 0 = circular and 1 = extremely elongated.

secondary fractures (Fig. 9c-e). This shows that individual fractures intersected a higher proportion of magma along one primary direction, and communication between fractures within a fracture band was limited to one or two neighbors (Fig. 9d). Hence, connectivity of the fractures would have favored fluid flow along the long axis of the fracture planes, rather than crossing between fractures within the same fracture band.

## 5. Discussion

### 5.1. Viscous to brittle deformation of a crystal mush

The microstructures described in this study outline a continuum of deformation features (from lowest to highest degree of deformation: porous flow bands, pore channels, and fracture bands; Table 1). Based on significant overlap in their characteristics, we conclude that they are preserved snapshots representing different stages of the same process: pore channels are found partially developed within porous flow bands (Fig. 3d), and remnants of porous flow bands are evident between the established pore channels (Fig. 2c & 4a). Furthermore, pore channels are arranged in a band orientated perpendicular to their long axis (Fig. 2c), similar to fracture bands (Fig. 2d & e). For these reasons, we propose a conceptual model that explains the described features as the result of sustained deformation applied to flow-banded magma when the magma was a ductile mush (Fig. 10). We will now discuss the magma rheology evolution based on published experimental work, our hypothesis for how the deformation features formed, and implications for magma outgassing in the Sandfell laccolith.

The sparse (~5 modal%), mm-scale euhedral plagioclase phenocrysts (Fig. 2) represent the earliest evidence of the Sandfell magma's evolution, indicating pre-emplacement plagioclase crystallization with a low nucleation rate and high growth rate (Fig. 10 bottom circle). In

contrast, the abundant microlites of alkali feldspar and iron oxides of the groundmass (Fig. 2a) formed during subsequent crystallization with high nucleation rates and low growth rates, which corresponds to a high degree of undercooling (Mollo and Hammer, 2017).

The concentration of groundmass quartz within the porous flow bands indicates the segregation of the magma into silica-richer and silica-poorer flow bands (Fig. 10 second circle from the bottom). Flow bands in magma have been suggested to form as a result of mechanical deformation (Gonnermann and Manga, 2005; Schall and van Heege, 2010). While it is no longer possible to determine the conditions of flow band formation in the Sandfell laccolith, deformation experiments show that around a crystal fraction of 45 to 55 %, melt-rich shear bands separate from magma (Pistone et al., 2012). The separation of the melt from the crystalline magma during shear would then naturally imply a compositional separation between melt- and silica-richer bands among more crystalline and silica-poorer bands. This compositional separation is expressed in terms of significant variations in quartz content between porous/pore channel and non-porous flow bands. The orientations of flow bands are shown in Witcher et al. (2024) to reflect the progressive change in growth mode of the Sandfell laccolith from the earliest, sill-like magma batch to the later doming and establishment of a trap-door fault along the northern margin. This observation rules out the occurrence of cryptic magma fragmentation during emplacement that has been proposed for volcanic conduits by Wadsworth et al. (2022) since such flow-band orientations would not have been preserved through the process of fragmentation. Experiments on flow banded magma have shown that the flow bands richer in melt remain at a lower bulk viscosity, given the absence of crystals (Kohlstedt et al., 2010). We therefore infer that the melt-rich flow bands at Sandfell localized continued shear.

The high concentration of quartz grains between the pores in porous flow bands, and the occurrence of larger pores exclusively between

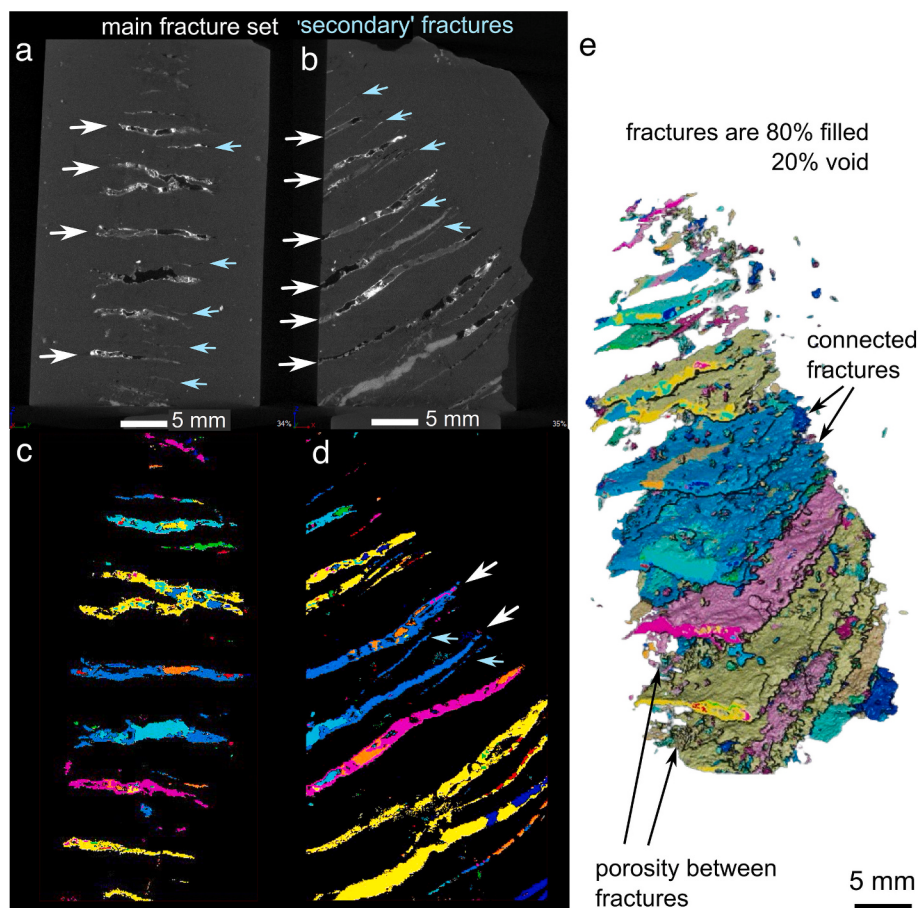


**Fig. 9.** Slices of  $\mu$ CT-scanned fracture band sample (thin section block of sample shown in Fig. 2e), in ZY plane (a) and ZX plane (b). Greyscale is the same as BSE images: black is void, white is Fe-oxides, dark grey is groundmass and mid-greys are mineral fillings. Primary and secondary fracture sets are indicated with white and light blue arrows, respectively. c, d) Connectivity of phases calculated from the scan, each color represents a connected phase. 20 % of the fracture volume is open space, 80 % is filled. e) 3D image of fracture band with groundmass removed, colored by connectivity. (For interpretation of the references to color in this figure legend, the reader is referred to the web version of this article.)

quartz grains, while smaller pores occur between the microlites (Fig. 3), indicate that the quartz aggregates and the microlites are key components in the formation of the porous flow bands. Typically, vesicles (that is, the solidified remnant of gas bubbles expanded within liquid) have smooth walls and spherical or ellipsoidal shapes (e.g., Fig. 3d). Pores within the viscous flow bands are dominantly irregular in shape and have rough walls, lined with euhedral and broken microlites (Fig. 2b). This texture has been produced in deformation experiments of microlite-rich synthetic magma, where a low degree of shear strain ( $\gamma = 0.4$ ) reoriented microlites and drove them into the bubble, destroying the smooth bubble wall (cf. Laumonier et al., 2011).

Based on analyses presented by Shea et al. (2010), and assuming the porosity within flow bands originated from bubble expansion, one argument for the development of flow band porosity is through the coalescence and/or collapse of bubbles. This would explain the concave tapering of the CVND curve at a larger size fraction and the normal elongation distribution (Fig. 8b & c). This is supported by the observation that in thin sections some areas of a porous flow band are vesicle-poor while others are vesicle-rich (e.g., Fig. 3d); variations in strain would likely promote coalescence in some areas and bubble collapse in others. Our observations agree with the deformation experiments of Laumonier et al. (2011), which show that bubbles migrated through the microlitic groundmass from areas of low strain towards areas of high strain.

We envisage porosity development in microlite-rich Sandfell magma under shear stress a viable process to explain the textures of the porous

flow bands (Figs. 3 & 10) in addition to bubble collapse. Critical soil mechanics describes the phenomenon of pore formation in the presence of rigid particles (Schofield and Wroth, 1968) and has been applied to magma rheology (Caricchi et al., 2007; Rutter et al., 2006). In fact, the textures in the porous flow bands resemble those of dilation bands in granular materials where stable solid-solid contact between grains can transmit tensile strain leading to void formation (Du Bernard et al., 2002; Gourlay and Dahle, 2007; Meylan et al., 2010; Petford et al., 2020). The solid-solid contacts—in case of the rhyolite magma, the microlites lining the quartz grains—can locally fracture (Fig. 3) (Forien et al., 2011), while the bulk system is behaving plastically (Petford et al., 2020). The reorganizing of the rigid particles—here, the quartz grains—then promotes a volume increase by pore formation at the points of maximum tensile stress. Hence, we envisage that porous flow bands formed in a similar way to dilation bands when the magma had crystallized to at least  $\phi_c = 0.7$  (Petford et al., 2020), and behaved as a poro-elastic mesh.

In granular materials, dilation band thickness increases with total strain (Sakaie et al., 2008) until a critical thickness, dictated by the granular material properties, is reached (Ries et al., 2007). This could explain why the Sandfell porous flow bands are of such regular thickness and spacing (e.g., Fig. 2a): The porous flow band thicknesses in the Sandfell laccolith are likely the result of the response of the magma's crystal fraction to strain, whereas the crystal fraction is a function of the earlier separation into flow bands (see above; Fig. 10 II & III).

Dilation of a poro-elastic mesh—in this case, microlite-rich

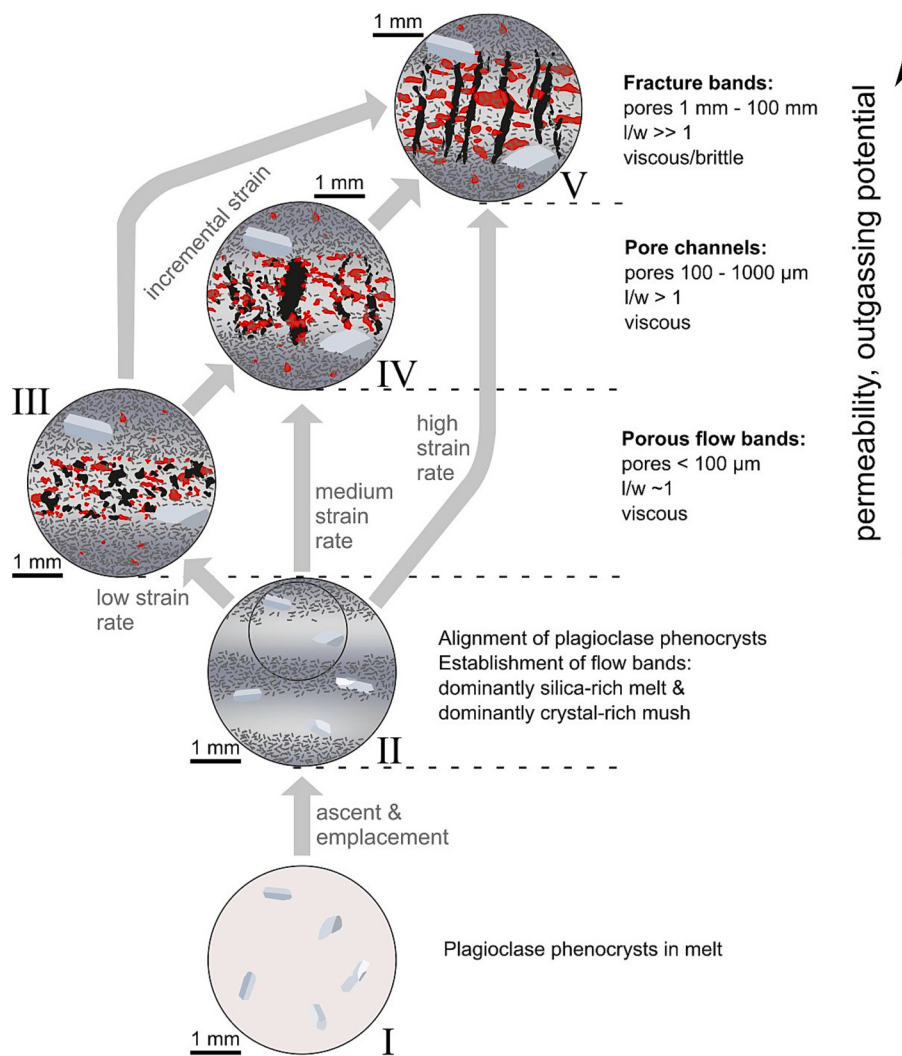


**Fig. 10.** Conceptual model of the porosity development in the Sandfell laccolith, explaining the observed textures as a result of either different strain rates or incremental strain applied to a flow-banded, crystal-rich magma. Color scale follows the thresholded BSE images in Figs. 3–5. Permeability and outgassing potential increases with increasing deformation.

magma—creates an increase in void volume between grains, and the associated negative pore pressure draws in nearby fluid (melt or gas) (Petford et al., 2020). The abundance of the interstitial melt phase in the porous flow bands (Fig. 3b) and pore channels (Fig. 4d) supports this argument. Dilatation banding is a process that entails strain softening and results in concentrating continued applied stress (Gourlay and Dahle, 2007). A phenomenon often associated with dilatation banding is cavitation, a process in ductile solids by which preexisting defects propagate, commonly at a solid particle interface, causing the material to 'tear' and form a cavity (Farquharson et al., 2016).

The cavitation is a response to a pressure drop which overcomes the cohesion or tensile strength of the material (Gruzdakov and Petrov, 2008). Most research on cavitation has been done in metallurgy (Nicolaou and Semiatin, 2007; Rappaz et al., 1999; Tanaka and Higashi, 2004) but it is increasingly discussed as a deformation mechanism in crystal-rich magmas (Farquharson et al., 2016; Furukawa and Uno, 2015; Petford et al., 2020; Smith et al., 2001).

Considering the mechanism of dilation banding and cavitation, we argue that the pore channels observed in the Sandfell laccolith formed in the following way (Fig. 10 IV): within the porous flow band plane, stress associated with magma intrusion created pressure differentials among the quartz grains and their immediate surroundings. These pressure contrasts were sufficient to propagate the dilated pores via cavitation,

and the increasingly densely packed microlites suspended in melt tore away from the larger quartz grains, propagating in the direction of the maximum principle stress (Fig. 4a). Pores continued to grow sub-parallel to the largest principle compressive stress ( $\sigma_1$ ) direction and opened parallel to the lowest principal compressive stress ( $\sigma_3$ ) direction (as shown in experiments by Van Der Molen and Paterson, 1979). The pore channels have a convex size distribution (Fig. 8d) and a decline in pores with  $\epsilon > 0.7$ . Their cumulative volumetric number densities decrease linearly with size fraction (Fig. 8b). Based on Shea et al. (2010), processes consistent with these trends are 'continuous/accelerating nucleation and growth'. Rather than bubbles increasing in volume by expanding, we argue that this trend is the result of the pores becoming stretched through cavitation.

As mentioned above, the pore space created by cavitation caused a pressure gradient which would have drawn in local fluids like residual melt (Koenders and Petford, 2000; Petford et al., 2020; Van Der Molen and Paterson, 1979). This likely accounts for some of the microlite-free, sub- to euhedral quartz within the elongated pores (Fig. 4b & 5e), often at the tips (Fig. 4b; 5d, inset) and, to varying degrees, rooted to anhedral quartz in the groundmass with more microlite inclusions (Fig. 4c & 6a). Since this sub- to euhedral, pore-filling quartz is identical to the groundmass quartz in terms of crystal structure (Raman; Supp. Mat. 1) and crystallization temperature (TitaniQ; Supp. Mat. 3), we envisage

quasi-simultaneous crystallization of groundmass quartz and pore-filling quartz, which, by definition, includes pore formation. Further evidence for decompression within the pore channels and fracture bands are the microbubbles preserved in the melt phase near some pore channels (e.g., Fig. 4e & f) and larger bubbles ( $<40\text{ }\mu\text{m}$ ) inside smaller fractures (e.g., Fig. 5g).

Our samples testify to a continuous transition from porous flow bands to pore channels to fracture bands (Fig. 10 incremental strain paths). Conceivably, fracture bands may have also formed by cavitation, as proposed by Smith et al. (2001) for the porosity features in dacite lava domes (see Fig. 5d in Smith et al., 2001) that exactly resemble the fracture bands in the Sandfell laccolith. However, while we acknowledge the likely role of cavitation in the formation of the pore channels, as discussed above, the fracture bands in the Sandfell laccolith (and also those in Fig. 5d of Smith et al., 2001) have a significantly more brittle appearance, as evidenced by *en echelon* arrays (Figs. 2e; 5c & d), and their higher aspect ratios (compare Fig. 2c with 2d & f). We, therefore, propose that there was a transition from ductile cavitation to brittle fracturing during the formation of the fracture bands (Fig. 10 V). As described by Raayai-Ardakani et al. (2019), cavitation and fracturing processes are closely related in soft materials, and pore expansion can abruptly switch between fracture-dominated and cavitation-dominated depending on strain rate. Incremental growth via cavitation and sudden, rapid growth via fracturing likely operated in tandem to form the deformation features seen in the Sandfell rhyolite (incremental strain paths in Fig. 10). The formation of fractures with very high aspect ratios and minimal porosity between fractures (like those in Fig. 2d) may have resulted from a high initial strain rate, which would have driven the viscous, crystal-rich magma to brittle failure without viscously deforming first (high strain rate path in Fig. 10). In that sense, strain rate is a key parameter in determining what type of deformation will take place in microcrystalline mush as well as in pure silicate melt.

To approximate the conditions required to develop fractures within the viscous crystalline rhyolite of Sandfell, we consider the 1991–1995 lava dome eruption on Unzen. Unzen lava dome samples exhibit cavitation textures closely resembling those in the Sandfell laccolith (Smith et al., 2001). Dacitic magma extruded endogenously in the second half of the Unzen eruption in 1993 for  $\sim 600$  days (Nakada et al., 1995). Ascent rates ( $u$ ) and conduit radii ( $L$ ) were calculated by Noguchi et al. (2008) to be  $\sim 0.002\text{ ms}^{-1}$  and  $\sim 5\text{ m}$ , respectively, at the peak of the 1993 dome-building phase. Wadsworth et al. (2018) use these parameters to estimate an average strain rate  $\langle\dot{\gamma}\rangle$  imparted on the magma, given by  $\langle\dot{\gamma}\rangle = u/L$ . With this, we can approximate that a strain rate of  $\langle\dot{\gamma}\rangle = 4 \times 10^{-4}\text{ s}^{-1}$  deformed the magma as it extruded from the conduit. Strain rates at this order of magnitude have been shown experimentally to viscously ‘tear’ dome lavas from Santiaguito (Guatemala) in tension at  $\sim 750\text{ }^{\circ}\text{C}$  (Hornby et al., 2019), which also aligns with the crystallization temperature of pore-filling quartz in the Sandfell rhyolite. While  $\langle\dot{\gamma}\rangle$  is a general approximation, it proves that deformation timescales required to initiate cavitation and fracture in intruding mushy magma are conceivable for conditions applicable to the formation of the Sandfell laccolith. Endogenous dome growth, such as at Sandfell, also creates a radially compressive stress environment that would localize pure shear on heterogeneities associated with separate magma pulses within the dome.

As the Sandfell magma degassed and developed porosity, local loss in volatiles of the remaining melt near the pores would have lowered the glass transition temperature ( $T_g$ ) of the remaining melt (Hess and Dingwell, 1996). As a result, the onset of brittle behavior in the degassed melt near the pores would have been reached at lower strain rates than the melt further from the pores (Webb and Dingwell, 1990). Continued emplacement-related stresses applied to the magma would have exceeded the strength of the melt phase at these degassed zones.

To further account for the brittle fracturing within bands, specifically the termination of fractures at the band margins, the higher porosity of

porous flow bands (with and without pore channels) caused a decrease in tensile strength compared to the more crystalline, less porous magma outside the flow band (cf. Heap et al., 2021). When the tensile strength was exceeded within the band, either from rapidly applied stress or gradual compression and shear, the material failed along existing weaknesses. As a consequence, fractures propagated vertically through the pores either by tensile fracturing or a combination of cavitation and fracturing. The fracture tips found in the Sandfell laccolith are branched and have gradational (diktytaxisitic) edges (Fig. 5). Similar morphologies have been experimentally produced by Oppenheimer et al. (2015) by injecting gas into golden syrup with  $>55\%$  solids in suspension. Suppose we assume a comparable mechanism in the Sandfell rhyolite magma. In that case, the exsolved volatiles would have contributed to the fractures’ propagation by pressurizing the open pores in a densely packed microcrystalline groundmass.

This mechanism resembles what has been suggested for the formation of tuffisites, where magma fracturing draws in volatiles and melt fragments (ash) into the developing fracture (Unwin et al., 2021). We therefore envisage that tuffisites may start in the same way as the fractures in the Sandfell laccolith, evidenced by the observed microscopic tuffosite textures (Fig. 4e). However, tuffosite propagation in the magma and into the host rock, driving melt fragmentation into ash particles, and subsequent viscous healing (Tuffen et al., 2003; Tuffen and Dingwell, 2005) indicate a higher melt fraction, higher strain rates, and potentially higher volatile contents creating higher internal pressure in tuffisites compared to Sandfell.

Regarding the stress regime during the formation of the deformation features described in this study, Witcher et al. (2024) showed that the Sandfell laccolith was constructed by the successive emplacement of several magma batches, resulting in different structural domains (see also Fig. 1). To account for the consistently microcrystalline texture, we infer for the Sandfell magma at the time of formation of the deformation features: Each magma batch likely had time to cool enough to develop into a microcrystalline mush before the next magma-batch injection. At the same time, each new batch intrusion would exert stress on previously emplaced magma mush and the surrounding rocks.

As all the deformation features except porous flow bands have distinct tensile characteristics (the width of the fractures and pores is widest in the center and pinches out at the tips; e.g., Figs. 2c, e; 4a, b; 5a; 6), and are oriented  $\sim 90^{\circ}$  to the band they are forming in (Fig. 2c-e), compression seems the likely dominant stress regime at the time of pore channel and fracture band formation. Antithetic Riedel shears occur at a maximum of  $75^{\circ}$  to the shear plane, and tension gashes occur at  $45^{\circ}$  (Dresen, 1991; Schmocker et al., 2003). We can therefore rule out that the tensile features within the Sandfell rhyolite are Riedel structures. While there was likely a component of simple shear, pure shear from compression was the dominant stress regime linked to intrusion inflation. The brittle transition from pore channels to fracture bands may likely have initiated more fractures between elongated pores (as the fractures are more closely spaced than the pore channels), but stress shadows kept a minimum distance between fractures.

In summary, there was a rheological contrast early on in the Sandfell rhyolite’s emplacement caused by the segregation of melt into flow bands within an increasingly microcrystalline mush. The cessation of magma batch intrusion allowed time for continued crystallization and cooling, at slower rates within the melt-rich shear bands compared to the bulk rhyolite. The shear bands contained melt enriched in silica, which resulted in a higher concentration of quartz among the microlites. Before the magma reached complete solidification, another batch of magma was injected below and imparted stress upon the now-mushy rhyolite. The stress localized within the softer material of the early flow bands, resulting in a range of deformation features that created porosity and permeability that could not extend out into the material of the stronger and more tightly packed crystalline rhyolite. If strain rates were high enough to exceed the tensile strength of the stronger mush, fractures could propagate and possibly join over- and underlying

rheologically softer bands, with or without developed porosity (e.g., Fig. 2d).

### 5.2. Magma de- and outgassing in the Sandfell laccolith

In the following, we will discuss how the development of a permeable network of pores and fractures within the crystal mush of the Sandfell laccolith influenced magma de- and outgassing.

It has been shown that magma ascending through the volcanic conduit has the greatest chance of outgassing adjacent to the conduit walls, where large degrees of simple shear are applied to the magma (Benson et al., 2012; Burgisser and Gardner, 2004; Colombier et al., 2022; Gonnermann and Manga, 2009; Lavallée et al., 2012; Okumura et al., 2010; Okumura and Sasaki, 2014; Saubin et al., 2016; Tuffen and Dingwell, 2005). As a consequence, tuffisites may form near the conduit walls, but heal quickly after they form (Farquharson et al., 2017; Wadsworth et al., 2021). Hence, magma outgassing is limited in space (to the conduit walls) and time (to the duration before tuffisite healing), so a significant volume of magma at the center of the conduit struggles to outgas during ascent. Still, ascending silicic magma is not always behaving explosively (e.g., during spine extrusion or laccolith intrusion), indicating that another, complementary mechanism for magma outgassing is needed.

In this study, we show that bulk outgassing of large volumes of silicic magma can be achieved through viscous to brittle deformation. In the Sandfell laccolith, extensive fracturing took place within most of the 0.6 km<sup>3</sup> of rhyolite at ~500 m depth, at a considerable distance from the host rock (Witcher et al., 2024). Even at strain rates associated with effusive dome growth ( $\leq 10^{-4}$  s<sup>-1</sup>; Section 5.1), the stress applied to the bulk of the Sandfell magma was sufficient to dilate, cavitate, and fracture as laccolith growth continued. The result of the near-solidus deformation was a permeable network with the potential for magma outgassing. In other words, permeability-enhancing brittle deformation in our model is within the bulk of the magma, and not restricted to the highly strained zone at the interface between the magma and the host rock.

Porous flow bands developed by one (or both) of the following mechanisms: 1) growth of bubbles within a melt-rich shear zone, which was subsequently dismantled from shearing of the microlite-rich groundmass. 2) Quartz crystallized within the melt-rich shear zone, and dilation-induced porosity developed from the expansion of quartz-quartz contacts under shear. Both mechanisms facilitate degassing of the surrounding melt, and porosity was connected enough to allow fluid flow ( $k = 2.05 \times 10^{-14}$  m<sup>2</sup>, Section 4.3). Dilation banding would have drawn in fluids from the surrounding crystalline network, further degassing the magma.

As pore channels developed through cavitation, nearby pores were assimilated, which would have increased the connectivity of porosity (Figs. 3d & 4a). The increasing pore volume had a negative pore pressure which would have drawn in more fluids from the surroundings, including the melt between microlites and creating the diktytaxitic textures (Figs. 4d & 5g). The oriented traces of pore channels seen in the exposed planes in outcrop (Fig. 1d) testify to the enhanced outgassing potential compared to the porous flow bands because connectivity is apparent at the macro scale. Evidence for fluids moving through the pore channels is provided by the euhedral-zoned quartz growing in the pore space (Figs. 5e & 6a). Consistency between pore-filling and groundmass Ti-in-quartz geothermometry results ( $718 \pm 60^\circ\text{C}$ ) leads us to conclude the migrating fluids were magmatic in origin, as opposed to a much cooler ( $<300^\circ\text{C}$ ) hydrothermal fluid later precipitating the pore-filling quartz.

The onset of fracture formation would have significantly increased the magma's outgassing abilities through the increasing surface area of the pore (fracture) and the connection of over- and underlying softer bands. More coherent magma was affected by open fractures—and more

quickly—than pore channels and flow bands. This would have accelerated the degassing of melt into the fractures, as shown by the preserved bubbles in the melt filling a fracture (Fig. 5g), and then aided outgassing through the increasingly anastomosing network of fracture bands. Fracture bands evolved the pore channel geometries into exaggerated 'stretched pennies' (Fig. 9). Given the minor connectivity between fractures in the same fracture band (at mm scale; Fig. 9c-e), permeability must have been anisotropic within a fracture band, preferring the long axis direction of each fracture, which, with the limited connectivity between fractures, can extend for several meters (Witcher et al., 2024).

In outcrop, single-set fracture bands up to 20 cm thick are observed (Fig. 1g), as well as fracture bands containing more than one fracture set (Fig. 2e). The higher surface area of large fracture bands and more complex porosity formed by multi-set fracture bands further increases their outgassing potential. Fracture bands of these types can occur in proximity, with interlayered coherent magma diminishing until only lenses remain. Outcrops like these are categorized as 'breccia' in the companion field study (Witcher et al., 2024) and represent the highest potential for outgassing preserved in the rhyolite. As proposed by Witcher et al. (2024), these large fracture bands and breccia are part of the continuum of deformation features observed in the Sandfell laccolith. However, the size and properties of samples of large fracture bands and breccia forced us to exclude them from this study. Still, the results of this study on porous flow bands to small fracture bands lead us to infer that large flow bands and breccia form by continued brittle deformation of the crystal mush, controlled by its rheology, crystal interactions, strain rate and finite strain applied through shearing of the sub-solidus magma (Fig. 10).

While the Sandfell laccolith was emplaced at ~500 m depth, the textures observed here have also been described in crystal-rich lava domes (in Japan: Unzen, Daisen, Yakedake; Smith et al., 2001) and other shallow laccoliths (in Argentina: Cerro Alquitran; Galland et al., 2023, and Cerro Bayo; Burchardt et al., 2019). We propose that deformation-induced outgassing can take place during late-stage magma emplacement, in areas not restricted to the volcanic conduit. Sub-solidus conditions (high crystal fraction) can enable the development of permeable networks in a large volume of the intrusion that facilitate outgassing. Preservation of the permeable fracture network in the andesitic Cerro Alquitran allowed bitumen to seep to the surface from depth (Galland et al., 2023), further exemplifying the potential in fracture bands for fluid transport.

In the case of the Sandfell laccolith, the low-deformation end-members (mm-scale porous flow bands) grade into larger, cm-scale pore channels, which grade into even larger, cm-dm-scale fracture bands. In outcrop, fracture bands can be so densely overlapping that coherent rhyolite only exists as lenses among the fractures. These brecciated zones are associated with large-scale magmatic structural domains that localized stress caused by magma batch emplacement, and also represent the highest potential for outgassing of the newly intruded magma. Hence, the mechanism of magma outgassing observed at Sandfell provides a means to efficiently outgas large volumes of magma that is not restricted in space and time.

## 6. Conclusions

The Sandfell laccolith in Eastern Iceland hosts a network of deformation features throughout its microcrystalline rhyolite. Here we have studied the microstructures of porous flow bands, elongated pore channels, and fracture bands to characterize the pore geometries and estimate the rheology of the magma at the time of their formation. Our results suggest all types of deformation features formed when the magma was in a microcrystalline mush state.

The evolution of magma rheology during ascent and successive magma batch emplacement would have recorded deformation through viscous (crystal-poor: flow bands, sheared bubbles), ductile (crystal-rich; dilation and cavitation), and brittle manners (crystal lock up and

fracture). The resulting textures of each material response would have continued to localize applied stress, which would have increased the degree of deformation within the magma, further localized stress, and ultimately affected the emplacement dynamics of the entire laccolith.

Hence, with this case study, we demonstrate that it is the complex material properties of the magma that control both the response to emplacement-related stresses and the outgassing of volatiles. The similarities between shallow laccoliths and lava domes regarding geometry, composition, and low confining pressure allow for comparison between the two environments. We can therefore apply these outgassing mechanisms to viscous effusive lava domes, and contribute incremental development of porosity throughout the bulk of the magma as a potential outgassing source versus limited to shear along conduit walls.

### CRediT authorship contribution statement

**Taylor Witcher:** Writing – review & editing, Writing – original draft, Visualization, Methodology, Investigation, Formal analysis, Data curation, Conceptualization. **Steffi Burchardt:** Writing – review & editing, Visualization, Supervision, Investigation, Funding acquisition, Conceptualization. **Tobias Mattsson:** Writing – review & editing, Visualization, Software, Methodology, Investigation, Formal analysis, Data curation. **Michael J. Heap:** Writing – review & editing, Supervision, Investigation. **Anne Pluymakers:** Writing – review & editing, Visualization, Software, Resources, Methodology, Formal analysis, Data curation. **Kai Li:** Writing – review & editing, Software, Methodology, Data curation. **Peter Lazor:** Resources, Methodology, Formal analysis.

### Declaration of competing interest

The authors declare that they have no known competing financial interests or personal relationships that could have appeared to influence the work reported in this paper.

### Acknowledgements

TW was funded by a Knut and Alice Wallenberg fellowship to SB (KAW2017-0153).

TM was funded by the Swedish Research Council grant (2019-06300).

M. Heap acknowledges support from the Institut Universitaire de France (IUF).

### Appendix A. Supplementary data

Supplementary data to this article can be found online at <https://doi.org/10.1016/j.jvolgeores.2025.108278>.

### Data availability

Data is shared in the supplementary materials.

### References

- Allibirov, M., Dingwell, D.B., 1996. Magma fragmentation by rapid decompression. *Nature* 380, 146–148.
- Allan, A.S.R., Barker, S.J., Millet, M.A., Morgan, D.J., Rooyakkers, S.M., Schipper, C.I., Wilson, C.J.N., 2017. A cascade of magmatic events during the assembly and eruption of a super-sized magma body. *Contrib. Mineral. Petrol.* 172 (7). <https://doi.org/10.1007/s00410-017-1367-8>.
- Arganda-Carreras, I., Kaynig, V., Rueden, C., Eliceiri, K.W., Schindelin, J., Cardona, A., Sebastian Seung, H., 2017. Trainable Weka Segmentation: a machine learning tool for microscopy pixel classification. *Bioinformatics* 33 (15), 2424–2426. <https://doi.org/10.1093/bioinformatics/btx180>.
- Barker, A.K., Troll, V.R., Carracedo, J.C., Nicholls, P.A., 2015. The magma plumbing system for the 1971 Teneguía eruption on La Palma, Canary Islands. *Contrib. Mineral. Petrol.* 170, 54. <https://doi.org/10.1007/s00410-015-1207-7>.
- Benson, P.M., Heap, M.J., Lavallée, Y., Flaws, A., Hess, K.U., Selvadurai, A.P.S., Dingwell, D.B., Schillinger, B., 2012. Laboratory simulations of tensile fracture development in a volcanic conduit via cyclic magma pressurisation. *Earth Planet. Sci. Lett.* 349–350, 231–239. <https://doi.org/10.1016/j.epsl.2012.07.003>.
- Birnbaum, J., Lev, E., Llewellyn, E.W., 2021. Rheology of three-phase suspensions determined via dam-break experiments. *Proc. Roy. Soc. A* 477. <https://doi.org/10.1098/rspa.2021.0394>.
- Burchardt, S., Mattsson, T., Palma, J.O., Galland, O., Almqvist, B., Mair, K., Jerram, D.A., Hammer, Ø., Sun, Y., 2019. Progressive growth of the Cerro Bayo Cryptodome, Chachahuén Volcano, Argentina—Implications for Viscous Magma emplacement. *J. Geophys. Res. Solid Earth*. <https://doi.org/10.1029/2019jb017543>.
- Burchardt, S., Óskarsson, V., Gustafsson, L.E., Berg, S.E., Riishuus, M.S., 2022. Geology of a Neogene caldera cluster in the Borgarfjörður eystrí-Loðmundarfjörður area, Eastern Iceland. *Volcanica* 5 (1), 133–161. <https://doi.org/10.30909/vol.05.01.133161>.
- Burgisser, A., Gardner, J.E., 2004. Experimental constraints on degassing and permeability in volcanic conduit flow. *Bull. Volcanol.* 67 (1), 42–56. <https://doi.org/10.1007/S00445-004-0359-5>.
- Caricchi, L., Burlini, L., Ulmer, P., Gerya, T., Vassalli, M., Papale, P., 2007. Non-Newtonian rheology of crystal-bearing magmas and implications for magma ascent dynamics. *Earth Planet. Sci. Lett.* 264 (3–4), 402–419. <https://doi.org/10.1016/j.epsl.2007.09.032>.
- Carrara, A., Burgisser, A., Bergantz, G.W., 2024. Numerical simulations of the mingling caused by a magma intruding a resident mush. *Volcanica* 7 (1), 89–104. <https://doi.org/10.30909/vol.07.01.89104>.
- Carter, L.C., Williamson, B.J., Tapster, S.R., Costa, C., Grime, G.W., Rollinson, G.K., 2021. Crystal mush dykes as conduits for mineralising fluids in the Yerington porphyry copper district, Nevada. *Commun. Earth Environ.* 2 (1). <https://doi.org/10.1038/s43247-021-00128-4>.
- Castro, J.M., Cordonnier, B., Tuffen, H., Tobin, M.J., Puskar, L., Martin, M.C., Bechtel, H.A., 2012. The role of melt-fracture degassing in defusing explosive rhyolite eruptions at volcán Chaitén. *Earth Planet. Sci. Lett.* 333–334, 63–69. <https://doi.org/10.1016/j.epsl.2012.04.024>.
- Champallier, R., Bystricky, M., Arbaret, L., 2008. Experimental investigation of magma rheology at 300 MPa: from pure hydrous melt to 76 vol.% of crystals. *Earth Planet. Sci. Lett.* 267 (3–4), 571–583. <https://doi.org/10.1016/j.epsl.2007.11.065>.
- Colombier, M., Bernard, B., Wright, H., Le Pennec, J.L., Cáceres, F., Cimarelli, C., Heap, M.J., Samaniego, P., Vasseur, J., Dingwell, D.B., 2022. Conduit processes in crystal-rich dacitic magma and implications for eruptive cycles at Guagua Pichincha volcano, Ecuador. *Bull. Volcanol.* 84 (12). <https://doi.org/10.1007/s00445-022-01612-1>.
- Cordonnier, B., Caricchi, L., Pistone, M., Castro, J., Hess, K.U., Gottschaller, S., Manga, M., Dingwell, D.B., Burlini, L., 2012. The viscous-brittle transition of crystal-bearing silicic melt: direct observation of magma rupture and healing. *Geology* 40 (7), 611–614. <https://doi.org/10.1130/G3914.1>.
- Dingwell, D.B., 1996. Volcanic dilemma: Flow or blow?. In: *Science* (Vol. 273, Issue 5278, pp. 1054–1055). American Association for the Advancement of Science. <https://doi.org/10.1126/science.273.5278.1054>.
- Dingwell, D.B., Webb, S.L., 1989. Structural relaxation in silicate melts and non-newtonian melt rheology in geologic processes. *Phys. Chem. Miner.* 16.
- Dresen, G., 1991. Stress distribution and the orientation of Riedel shears. *Tectonophysics* 188, 239–247.
- Du Bernard, X., Eichhubl, P., Aydin, A., 2002. Dilation Bands: A New Form of Localized Failure in Granular Media. *Geophysical Research Letters* 29 (24), 29-1–29-4. <https://doi.org/10.1029/2002GL015966>.
- Eichelberger, J.C., Carrigan, C.R., Westrich, H.R., Price, R.H., 1986. Non-explosive silicic volcanism. *Nature* 323 (6089), 598–602. <https://doi.org/10.1038/323598a0>.
- Farquharson, J.I., Heap, M.J., Lavallée, Y., Varley, N.R., Baud, P., 2016. Evidence for the development of permeability anisotropy in lava domes and volcanic conduits. *J. Volcanol. Geotherm. Res.* <https://doi.org/10.1016/j.jvolgeores.2016.05.007>.
- Farquharson, J.I., Wadsworth, F.B., Heap, M.J., Baud, P., 2017. Time-dependent permeability evolution in compacting volcanic fracture systems and implications for gas overpressure. *J. Volcanol. Geotherm. Res.* 339, 81–97. <https://doi.org/10.1016/j.jvolgeores.2017.04.025>.
- Forien, M., Arbaret, L., Burgisser, A., Champallier, R., 2011. Experimental constraints on shear-induced crystal breakage in magmas. *J. Geophys. Res. Solid Earth* 116 (8). <https://doi.org/10.1029/2010JB008026>.
- Furukawa, K., Uno, K., 2015. Origin and deformation of high porosity bands in the Takanoobane Rhyolite lava of Aso volcano, Japan. *J. Volcanol. Geotherm. Res.* 305, 76–83. <https://doi.org/10.1016/j.jvolgeores.2015.09.021>.
- Galland, O., Villar, H.J., Mescua, J., Jerram, D.A., Midtkandal, I., Palma, J.O., Planke, S., Zanella, A., 2023. The Long-Term Legacy of Subvolcanic Intrusions on Fluid Migration in Sedimentary Basins: The Cerro Alquitrán Case Study, Northern Neuquén Basin, Basin Research, Argentina. <https://doi.org/10.1111/bre.12782>.
- Ghiorso, M.S., Gualda, G.A.R., 2013. A method for estimating the activity of titania in magmatic liquids from the compositions of coexisting rhombohedral and cubic iron-titanium oxides. *Contrib. Mineral. Petrol.* 165, 73–81. <https://doi.org/10.1007/s00410-012-0792-y>.
- Giachetti, T., Gonnermann, H.M., Gardner, J.E., Burgisser, A., Hajimirza, S., Earley, T.C., Truong, N., Toledo, P., 2019. Bubble Coalescence and Percolation Threshold in Expanding Rhyolitic Magma. *Geochem. Geophys. Geosyst.* 20 (2), 1054–1074. <https://doi.org/10.1029/2018GC008006>.
- Gibson, I.L., 1963. The Reydarfjordur Acid Volcano Centre of Eastern Iceland. *University of London*.
- Gibson, I.L., Kinsman, D.J.J., Walker, G.P.L., 1966. Geology of the Fáskrúðsfjörður Area, Eastern Iceland. *Visindafélag Íslanda*.

- Giordano, D., Romano, C., Papale, P., Dingwell, D.B., 2004. The viscosity of trachytes, and comparison with basalts, phonolites, and rhyolites. *Chem. Geol.* 213 (1–3), 49–61. <https://doi.org/10.1016/j.chemgeo.2004.08.032>.
- Gonnermann, H.M., Manga, M., 2003. Explosive volcanism may not be an inevitable consequence of magma fragmentation. *Nature* 426 (6965), 432–435. <https://doi.org/10.1038/nature02138>.
- Gonnermann, H.M., Manga, M., 2005. Flow banding in obsidian: a record of evolving textual heterogeneity during magma deformation. *Earth Planet. Sci. Lett.* 236 (1–2), 135–147. <https://doi.org/10.1016/j.epsl.2005.04.031>.
- Gonnermann, H.M., Manga, M., 2009. Dynamics of magma ascent in the volcanic conduit. In: *Modeling Volcanic Processes: The Physics and Mathematics of Volcanism*. Cambridge University Press, pp. 55–84. <https://doi.org/10.1017/CBO9781139021562.004>.
- Gourlay, C.M., Dahle, A.K., 2007. Dilatant shear bands in solidifying metals. *Nat. Lett.* 445. <https://doi.org/10.1038/nature05426>.
- Gruzdov, A.A., Petrov, Y.V., 2008. Cavitation breakup of low-and high-viscosity liquids. *Tech. Phys.* 53 (3), 291–295. <https://doi.org/10.1134/s106378420803002x>.
- Hawkes, L., Hawkes, H.K., 1933. The Sandfell Laccolith and “Dome of Elevation.”. *Q. J. Geol. Soc. Lond.* 89, 379–400.
- Heap, M.J., Kennedy, B.M., 2016. Exploring the scale-dependent permeability of fractured andesite. *Earth Planet. Sci. Lett.* 447, 139–150. <https://doi.org/10.1016/j.epsl.2016.05.004>.
- Heap, M.J., Kushnir, A.R.L., Gilg, H.A., Wadsworth, F.B., Reuschlé, T., Baud, P., 2017. Microstructural and petrophysical properties of the Permo-Triassic sandstones (Buntsandstein) from the Soultz-sous-Forêts geothermal site (France). *Geotherm. Energy* 5 (1). <https://doi.org/10.1186/s40517-017-0085-9>.
- Heap, M.J., Tuffen, H., Wadsworth, F.B., Reuschlé, T., Castro, J.M., Schipper, C.I., 2019. The Permeability Evolution of Tuffisites and Implications for Outgassing through Dense Rhyolitic Magma. *J. Geophys. Res. Solid Earth*. <https://doi.org/10.1029/2018JB017035>, 2018JB017035.
- Heap, M.J., Wadsworth, F.B., Heng, Z., Xu, T., Griffiths, L., Aguilar Velasco, A., Vairé, E., Vistour, M., Reuschlé, T., Troll, V.R., Deegan, F.M., Tang, C., 2021. The tensile strength of volcanic rocks: experiments and models. *J. Volcanol. Geotherm. Res.* 418. <https://doi.org/10.1016/j.jvolgeores.2021.107348>.
- Heiken, G., Wohletz, K., Eichelberger, J., 1988. Fracture fillings and intrusive pyroclasts, Inyo Domes, California. *J. Geophys. Res.* 93 (B5), 4335–4350. <https://doi.org/10.1029/JB093IB05P04335>.
- Hess, K.-U., Dingwell, D.B., 1996. Viscosities of hydrous leucogranitic melts: a non-Arrhenian model. *Am. Mineral.* 81, 1297–1300.
- Hess, K.-U., Dingwell, D.B., Gennaro, C., Mincione, V., 2001. Viscosity-temperature behaviour of dry melts in the Qz-Ab-or system. *Chem. Geol.* 174, 133–142. [www.elsevier.com/locate/chemgeo](http://www.elsevier.com/locate/chemgeo).
- Holness, M.B., 2018. Melt segregation from silicic crystal mushes: a critical appraisal of possible mechanisms and their microstructural record. *Contrib. Mineral. Petrol.* 173, 48. <https://doi.org/10.1007/s00410-018-1465-2>.
- Holness, M.B., Bunbury, J.M., 2006. Insights into continental rift-related magma chambers: Cognate nodules from the Kula Volcanic Province, Western Turkey. *J. Volcanol. Geotherm. Res.* 153 (3–4), 241–261. <https://doi.org/10.1016/j.jvolgeores.2005.12.004>.
- Holtzman, B.K., Groebner, N.J., Zimmerman, M.E., Ginsberg, S.B., Kohlstedt, D.L., 2003. Stress-driven melt segregation in partially molten rocks. *Geochem. Geophys. Geosyst.* 4 (5). <https://doi.org/10.1029/2001GC000258>.
- Hornby, A.J., Lavallée, Y., Kendrick, J.E., De Angelis, S., Lamur, A., Lamb, O.D., Rietbrock, A., Chigna, G., 2019. Brittle-Ductile Deformation and Tensile Rupture of Dome Lava during inflation at Santiaguito, Guatemala. *J. Geophys. Res. Solid Earth* 124 (10), 10107–10131. <https://doi.org/10.1029/2018JB017253>.
- Jaupart, C., Allègre, C.J., 1991. Gas content, eruption rate and instabilities of eruption regime in silicic volcanoes. *Earth Planet. Sci. Lett.* 102 (3–4), 413–429. [https://doi.org/10.1016/0012-821X\(91\)90032-D](https://doi.org/10.1016/0012-821X(91)90032-D).
- Katz, R.F., Spiegelman, M., Holtzman, B., 2006. The dynamics of melt and shear localization in partially molten aggregates. *Nat. Lett.* 442. <https://doi.org/10.1038/nature05039>.
- Koenders, M.A., Petford, N., 2000. Quantitative analysis and scaling of sheared granitic magmas. *Geophys. Res. Lett.* 27 (8), 1231–1234. <https://doi.org/10.1029/1999GL011118>.
- Kohlstedt, D.L., Zimmerman, M.E., Mackwell, S.J., 2010. Stress-driven Melt Segregation in Partially Molten Feldspathic Rocks. *J. Petrol.* 51 (1 & 2), 9–19. <https://doi.org/10.1093/petrology/egp043>.
- Kushnir, A.R.L., Martel, C., Champallier, R., Arbaret, L., 2017. In situ confirmation of permeability development in shearing bubble-bearing melts and implications for volcanic outgassing. *Earth Planet. Sci. Lett.* 458, 315–326. <https://doi.org/10.1016/j.epsl.2016.10.053>.
- Lamur, A., Kendrick, J.E., Wadsworth, F.B., Lavallée, Y., 2019. Fracture healing and strength recovery in magmatic liquids. *Geology* 47 (3), 195–198. <https://doi.org/10.1130/G45512.1>.
- Laumonier, M., Arbaret, L., Burgisser, A., Champallier, R., 2011. Porosity redistribution enhanced by strain localization in crystal-rich magmas. *Geology* 39 (8), 715–718. <https://doi.org/10.1130/G31803.1>.
- Lavallée, Y., Meredith, P.G., Dingwell, D.B., Hess, K.U., Wassermann, J., Cordonnier, B., Gerik, A., Krull, J.H., 2008. Seismogenic lavas and explosive eruption forecasting. *Nature* 453 (7194), 507–510. <https://doi.org/10.1038/nature06980>.
- Lavallée, Y., Benson, P.M., Heap, M.J., Flaws, A., Hess, K.-U., Dingwell, D.B., 2012. Volcanic conduit failure as a trigger to magma fragmentation. *Bull. Volcanol.* 74, 11–13. <https://doi.org/10.1007/s00445-011-0544-2>.
- Lejeune, A.M., Bottinga, Y., Trull, T.W., Richet, P., 1999. Rheology of bubble-bearing magmas. *Earth Planet. Sci. Lett.* 166, 71–84.
- Llewellyn, E.W., Mader, H.M., Wilson, S.D.R., 2002. The rheology of a bubbly liquid. *Proc. Roy. Soc. Lond. A* 458, 987–1016. <https://doi.org/10.1098/rspa.2001.0924>.
- Mader, H.M., Llewellyn, E.W., Mueller, S.P., 2013. The Rheology of Two-Phase Magmas: A Review and Analysis. <https://doi.org/10.1016/j.jvolgeores.2013.02.014>.
- Marsh, B., 2004. A magmatic mush column rosetta stone: The mcmurdo dry valleys of antarctica. *Eos* 85 (47). <https://doi.org/10.1029/2004EO470001>.
- Marsh, B.D., 1988. Crystal size distribution (CSD) in rocks and the kinetics and dynamics of crystallization I. Theory. *Contrib. Mineral. Petrol.* 99, 277–291.
- Martin, E., Sigmarsson, O., 2010. Thirteen million years of silicic magma production in Iceland: Links between petrogenesis and tectonic settings. *Lithos* 116 (1–2), 129–144. <https://doi.org/10.1016/J.LITHOS.2010.01.005>.
- Martin, E., Paquette, J.L., Bosse, V., Ruffet, G., Tiepolo, M., Sigmarsson, O., 2011. Geodynamics of rift-plume interaction in Iceland as constrained by new 40 Ar/39 Ar and in situ U-Pb zircon ages. *Earth Planet. Sci. Lett.* 311, 28–38. <https://doi.org/10.1016/j.epsl.2011.08.036>.
- Mattsson, T., Burchardt, S., Almqvist, B.S.G., Ronchin, E., 2018. Syn-emplacement fracturing in the sandfell laccolith, eastern Iceland—implications for rhyolite intrusion growth and volcanic hazards. *Front. Earth Sci.* 6. <https://doi.org/10.3389/feart.2018.00005>.
- Meylan, B., Terzi, S., Gourlay, C.M., Suéry, M., Dahle, A.K., 2010. Development of shear bands during deformation of partially solid alloys. *Scr. Mater.* 63, 1185–1188. <https://doi.org/10.1016/j.scriptamat.2010.08.032>.
- Mollo, S., Hammer, J.E., 2017. Dynamic crystallization in magmas. *Eur. Mineral. Union Notes Mineral.* 16, 373–418. <https://doi.org/10.1180/EMU-notes.16.12>.
- Nakada, S., Miyake, Y., Sato, H., Oshima, O., Fujinawa, A., 1995. Endogenous growth of dacite dome at Unzen volcano (Japan), 1993–1994. *Geology* 23 (2), 157–160. <http://pubs.geoscienceworld.org/gsa/geology/article-pdf/23/2/157/3515600/10091-7613-23-2-157.pdf>.
- Nicolaou, P.D., Semiatin, S.L., 2007. Effect of Strain-path reversal on microstructure evolution and cavitation during hot torsion testing of Ti-6Al-4V. *Metall. Mater. Trans. A* 38A. <https://doi.org/10.1007/s11661-007-9343-y>.
- Noguchi, S., Toramaru, A., Nakada, S., 2008. Relation between microlite textures and discharge rate during the 1991–1995 eruptions at Unzen, Japan. *J. Volcanol. Geotherm. Res.* 175 (1–2), 141–155. <https://doi.org/10.1016/j.jvolgeores.2008.03.025>.
- Okumura, S., Sasaki, O., 2014. Permeability reduction of fractured rhyolite in volcanic conduits and its control on eruption cyclicity. *Geology* 42 (10), 843–846. <https://doi.org/10.1130/G35855.1>.
- Okumura, S., Nakamura, M., Takeuchi, S., Tsuchiyama, A., Nakano, T., Uesugi, K., 2009. Magmatic deformation may induce non-explosive volcanism via degassing through bubble networks. *Earth Planet. Sci. Lett.* 281 (3–4), 267–274. <https://doi.org/10.1016/j.epsl.2009.02.036>.
- Okumura, S., Nakamura, M., Nakano, T., Uesugi, K., Tsuchiyama, A., 2010. Shear deformation experiments on vesicular rhyolite: Implications for brittle fracturing, degassing, and compaction of magmas in volcanic conduits. *J. Geophys. Res.* 115 (B6), B06201. <https://doi.org/10.1029/2009JB006904>.
- Okumura, S., Kushnir, A.R.L., Martel, C., Champallier, R., Thibault, Q., Takeuchi, S., 2016. Rheology of crystal-bearing natural magmas: Torsional deformation experiments at 800 °C and 100 MPa. *J. Volcanol. Geotherm. Res.* 328, 237–246. <https://doi.org/10.1016/J.JVOLGEORES.2016.11.009>.
- Oppenheimer, J., Rust, A.C., Cashman, K.V., Sandnes, B., 2015. Gas migration regimes and outgassing in particle-rich suspensions. *Frontiers. Physics* 3 (AUG). <https://doi.org/10.3389/fphy.2015.00060>.
- Padilla, A.J., de Miller, C.F., Guadalupe, G.A., Furbish, D.J., Clarke, J.H., Hornberger, G.M., 2015. Elemental and Isotopic Geochemistry of Crystal-Melt Systems: Elucidating the Construction and Evolution of Silicic Magmas in the Shallow Crust, Using Examples from Southeast Iceland and Southwest USA. *Vanderbilt University*.
- Papale, P., 1999. Strain-induced magma fragmentation in explosive eruptions. *Nature* 397, 425–428.
- Parmigiani, A., Huber, C., Bachmann, O., 2014. Mushmicrophysics and the reactivation of crystal-rich magma reservoirs. *J. Geophys. Res. Solid Earth* 119 (8), 6308–6322. <https://doi.org/10.1002/2014JB011124>.
- Paulatto, M., Hooft, E.E.E., Chrakiewicz, K., Heath, B., Toomey, D.R., Morgan, J.V., 2022. Advances in seismic imaging of magma and crystal mush. In: *Frontiers in Earth Science*, vol. 10. *Frontiers Media S.A.* <https://doi.org/10.3389/feart.2022.970131>.
- Petford, N., Koenders, M.A., Clemens, J.D., 2020. Igneous differentiation by deformation. *Contrib. Mineral. Petrol.* 175 (5). <https://doi.org/10.1007/s00410-020-1674-3>.
- Pistone, M., Caricchi, L., Ulmer, P., Burlini, L., Ardia, P., Reusser, E., Marone, F., Arbaret, L., 2012. Deformation experiments of bubble- and crystal-bearing magmas: Rheological and microstructural analysis. *J. Geophys. Res. Solid Earth* 117 (5). <https://doi.org/10.1029/2011JB008986>.
- Pistone, M., Arzilli, F., Dobson, K.J., Cordonnier, B., Reusser, E., Ulmer, P., Marone, F., Whittington, A.G., Mancini, L., Fife, J.L., Blundy, J.D., 2015. Gas-driven filter pressing in magmas: Insights into in-situ melt segregation from crystal mushes. *GEOLOGY* 43. <https://doi.org/10.1130/G36766.1>.
- Raayai-Ardakani, S., Rachelle Earl, D., Cohen, T., 2019. The intimate relationship between cavitation and fracture. *Soft Matter* 15 (25), 4991–5176. <https://doi.org/10.1039/c9sm00570f>.
- Rappaz, M., Drezet, J.-M., Gremaud, M., 1999. A New Hot-Tearing Criterion, Vol. 30.
- Ries, A., Wolf, D.E., Unger, T., 2007. Shear zones in granular media: Three-dimensional contact dynamics simulation. *Phys. Rev. E Stat. Nonlinear Soft Matter Phys.* 76 (5). <https://doi.org/10.1103/PhysRevE.76.051301>.
- Rust, A.C., Manga, M., 2002. Effects of bubble deformation on the viscosity of dilute suspensions. *J. Non-Newtonian Fluid Mech.* 104, 53–63.

- Rust, A.C., Manga, M., Cashman, K.V., 2003. Determining flow type, shear rate and shear stress in magmas from bubble shapes and orientations. *J. Volcanol. Geotherm. Res.* 122, 111–132. [www.elsevier.com/locate/jvolgeores](http://www.elsevier.com/locate/jvolgeores).
- Rust, A.C., Cashman, K.V., Wallace, P.J., 2004. Magma degassing buffered by vapor flow through brecciated conduit margins. *Geology* 349–352. <https://doi.org/10.1130/G20388.1>.
- Rutter, E.H., Brodie, K.H., Irving, D.H., 2006. Flow of synthetic, wet, partially molten “granite” under undrained conditions: an experimental study. *J. Geophys. Res. Solid Earth* 111 (6). <https://doi.org/10.1029/2005JB004257>.
- Sakaie, K., Fenistein, D., Carroll, T.J., Van Heeke, M., Umbanhowar, P., 2008. MR imaging of Reynolds' dilatancy in the bulk of smooth granular flows. *EPL* 84 (3). <https://doi.org/10.1209/0295-5075/84/38001>.
- Saubin, E., Tuffen, H., Gurioli, L., Owen, J., Castro, J.M., Berlo, K., McGowan, E.M., Schipper, C.I., Wehbe, K., 2016. Conduit dynamics in transitional rhyolitic activity recorded by tuffisite vein textures from the 2008–2009 Chaitén Eruption. *Front. Earth Sci.* 4, 59. <https://doi.org/10.3389/feart.2016.00059>.
- Schall, P., van Heeke, M., 2010. Shear bands in matter with granularity. *Annu. Rev. Fluid Mech.* 42 (1), 67–88. <https://doi.org/10.1146/annurev-fluid-121108-145544>.
- Schmocker, M., Bystricky, M., Kunze, K., Burlini, L., Stünitz, H., Burg, J.-P., 2003. Granular flow and Riedel band formation in water-rich quartz aggregates experimentally deformed in torsion. *J. Geophys. Res. Solid Earth* 108 (B5). <https://doi.org/10.1029/2002jb001958>.
- Schofield, A., Wroth, P., 1968. *Critical State Soil Mechanics*. McGraw-Hill.
- Shea, T., Houghton, B.F., Gurioli, L., Cashman, K.V., Hammer, J.E., Hobden, B.J., 2010. Textural studies of vesicles in volcanic rocks: an integrated methodology. *J. Volcanol. Geotherm. Res.* 190 (3–4), 271–289. <https://doi.org/10.1016/j.jvolgeores.2009.12.003>.
- Shields, J.K., Mader, H.M., Pistone, M., Caricchi, L., Floess, D., Putlitz, B., 2014. Strain-induced outgassing of three-phase magmas during simple shear. *J. Geophys. Res. Solid Earth* 119 (9), 6936–6957. <https://doi.org/10.1002/2014JB011111>.
- Sigmundsson, F., Einarsson, P., Rut Hjartardóttir, Á., Drouin, V., Jónsdóttir, K., Árnadóttir, T., Geirsson, H., Hreinsdóttir, S., Li, S., Ófeigsson, G., 2020. Geodynamics of Iceland and the signatures of plate spreading. *J. Volcanol. Geotherm. Res.* 391. <https://doi.org/10.1016/j.jvolgeores.2018.08.014>.
- de Silva, S.L., 1989. The origin and significance of crystal rich inclusions in pumices from two Chilean ignimbrites. *Geol. Mag.* 126 (2), 159–175. <https://doi.org/10.1017/S0016756800006300>.
- Smith, J.V., Miyake, Y., Oikawa, T., 2001. Interpretation of porosity in dacite lava domes as ductile-brittle failure textures. *J. Volcanol. Geotherm. Res.* 112 (1–4), 25–35. [https://doi.org/10.1016/S0377-0273\(01\)00232-3](https://doi.org/10.1016/S0377-0273(01)00232-3).
- Sparks, R.S.J., 2003. Dynamics of magma degassing. *Geol. Soc. Lond. Spec. Publ.* 213 (1), 5–22. <https://doi.org/10.1144/GSL.SP.2003.213.01.02>.
- Sparks, R.S.J., Annen, C., Blundy, J.D., Cashman, K.V., Rust, A.C., Jackson, M.D., 2019a. Formation and dynamics of magma reservoirs. In: *Philosophical Transactions of the Royal Society a: Mathematical, Physical and Engineering Sciences*, vol. 377, Issue 2139. Royal Society Publishing. <https://doi.org/10.1098/rsta.2018.0019>.
- Sparks, R.S.J., Annen, C., Blundy, J.D., Cashman, K.V., Rust, A.C., Jackson, M.D., 2019b. Formation and dynamics of magma reservoirs. *Philosop. Transact. Roy. Soc. A* 377. <https://doi.org/10.1098/rsta.2018.0019>.
- Tait, S.R., 1988. Contributions to Mineralogy and Petrology Samples from the crystallising boundary layer of a zoned magma chamber. *Contrib. Mineral. Petrol.* 100, 470–483.
- Tanaka, T., Higashi, K., 2004. Cavitation behavior in superplastically deformed Zn-22 mass%Al alloy at room temperature. *Mater. Trans.* 45 (8).
- Tuffen, H., Dingwell, D., 2005. Fault textures in volcanic conduits: evidence for seismic trigger mechanisms during silicic eruptions. *Bull. Volcanol.* 67 (4), 370–387. <https://doi.org/10.1007/s00445-004-0383-5>.
- Tuffen, H., Dingwell, D.B., Pinkerton, H., 2003. Repeated fracture and healing of silicic magma generate flow banding and earthquakes? *Geology* 3. <https://pubs.geoscienceworld.org/gsa/geology/article-pdf/31/12/1089/3525964/i0091-7613-31-12-1089.pdf>.
- Tuffen, H., Smith, R., Sammonds, P.R., 2008. Evidence for seismogenic fracture of silicic magma. *Nat. Lett.* 453, 511–514. <https://doi.org/10.1038/nature06989>.
- Unwin, H.E., Tuffen, H., Phillips, E., Wadsworth, F.B., James, M.R., 2021. Pressure-Driven opening and filling of a Volcanic Hydrofracture Recorded by Tuffisite at Húsafell, Iceland: a potential Seismic Source. *Front. Earth Sci.* 9. <https://doi.org/10.3389/feart.2021.668058>.
- Van Der Molen, I., Paterson, M.S., 1979. Experimental deformation of partially-melted granite. *Contrib. Mineral. Petrol.* 70, 318.
- Wadsworth, F.B., Witcher, T., Vossen, C.E.J., Hess, K.U., Unwin, H.E., Scheu, B., Castro, J.M., Dingwell, D.B., 2018. Combined effusive-explosive silicic volcanism straddles the multiphase viscous-to-brittle transition. *Nature. Communications* 9 (1). <https://doi.org/10.1038/s41467-018-07187-w>.
- Wadsworth, F.B., Vasseur, J., Llewellyn, E.W., Brown, R.J., Tuffen, H., Gardner, J.E., Kendrick, J.E., Lavallée, Y., Dobson, K.J., Heap, M.J., Dingwell, D.B., Hess, K.-U., Schauroth, J., Von Aulock, F.W., Kushnir, A.R.L., Marone, F., 2021. A model for permeability evolution during volcanic welding. *J. Volcanol. Geotherm. Res.* 409. <https://doi.org/10.1016/j.jvolgeores.2020.107118>.
- Wadsworth, F.B., Llewellyn, E.W., Castro, J.M., Tuffen, H., Schipper, C.I., Gardner, J.E., Vasseur, J., Foster, A., Damby, D.E., McIntosh, I.M., Boettcher, S., Unwin, H.E., Heap, M.J., Farquharson, J.I., Dingwell, D.B., Iacovino, K., Paisley, R., Jones, C., Whattam, J., 2022. A reappraisal of explosive-effusive silicic eruption dynamics: syn-eruptive assembly of lava from the products of cryptic fragmentation. *J. Volcanol. Geotherm. Res.* 432, 107672. <https://doi.org/10.1016/j.jvolgeores.2022.107672>.
- Walker, G.P.L., 1966. Acid volcanic rocks in Iceland. *Bull. Volcanol.* 29 (1), 375–402. <https://doi.org/10.1007/BF02597164>.
- Walker, G.P.L., 1974. The structure of Eastern Iceland. In: Kristjansson, L. (Ed.), *Geodynamics of Iceland and the North Atlantic Area*, vol. 11. D. Reidel Publishing Company, pp. 177–188.
- Walte, N.P., Rubie, D.C., Bons, P.D., Frost, D.J., 2011. Deformation of a crystalline aggregate with a small percentage of high-dihedral-angle liquid: Implications for core-mantle differentiation during planetary formation. *Earth Planet. Sci. Lett.* 305 (1–2), 124–134. <https://doi.org/10.1016/j.epsl.2011.02.049>.
- Wark, D.A., Watson, E.B., 2006. TitaniQ: a titanium-in-quartz geothermometer. *Contrib. Mineral. Petrol.* 152 (6), 743–754. <https://doi.org/10.1007/s00410-006-0132-1>.
- Webb, S.L., Dingwell, D.B., 1990. The onset of non-newtonian rheology of silicate melts a fiber elongation study. *Phys. Chem. Miner.* 17, 125–132.
- Witcher, T., Burchardt, S., Mattsson, T., Heap, M.J., McCarthy, W., 2024. Development of permeable networks in a shallow rhyolite intrusion. Part 1: field evidence. *Submitt. J. Volcanol. Geother. Res.* 454, 108166.
- Zimmerman, M.E., Kohlstedt, D.L., 2004. Rheological properties of partially molten lherzolite. *J. Petrol.* 45 (2), 275–298. <https://doi.org/10.1093/petrology/egg089>.
- Zorn, E.U., Walter, T.R., Heap, M.J., Kueppers, U., 2020. Insights into lava dome and spine extrusion using analogue sandbox experiments. *Earth Planet. Sci. Lett.* 551, 116571. <https://doi.org/10.1016/j.epsl.2020.116571>.